# In-Flight Wing Pressure Distributions for the NASA F/A-18A High Alpha Research Vehicle

Mark C. Davis and John A. Saltzman
NASA Dryden Flight Research Center
Edwards, California

March 2000

The NASA STI Program Office...in Profile

Since its founding, NASA has been dedicated to the advancement of aeronautics and space science. The NASA Scientific and Technical Information (STI) Program Office plays a key part in helping NASA maintain this important role.

The NASA STI Program Office is operated by Langley Research Center, the lead center for NASA's scientific and technical information. The NASA STI Program Office provides access to the NASA STI Database, the largest collection of aeronautical and space science STI in the world. The Program Office is also NASA's institutional mechanism for disseminating the results of its research and development activities. These results are published by NASA in the NASA STI Report Series, which includes the following report types:

- TECHNICAL PUBLICATION. Reports of completed research or a major significant phase of research that present the results of NASA programs and include extensive data or theoretical analysis. Includes compilations of significant scientific and technical data and information deemed to be of continuing reference value. NASA's counterpart of peer-reviewed formal professional papers but has less stringent limitations on manuscript length and extent of graphic presentations.

- TECHNICAL MEMORANDUM. Scientific and technical findings that are preliminary or of specialized interest, e.g., quick release reports, working papers, and bibliographies that contain minimal annotation. Does not contain extensive analysis.

- CONTRACTOR REPORT. Scientific and technical findings by NASA-sponsored contractors and grantees.

- CONFERENCE PUBLICATION. Collected papers from scientific and technical conferences, symposia, seminars, or other meetings sponsored or cosponsored by NASA.

- SPECIAL PUBLICATION. Scientific, technical, or historical information from NASA programs, projects, and mission, often concerned with subjects having substantial public interest.

- TECHNICAL TRANSLATION. English-language translations of foreign scientific and technical material pertinent to NASA's mission.

Specialized services that complement the STI Program Office's diverse offerings include creating custom thesauri, building customized databases, organizing and publishing research results...even providing videos.

For more information about the NASA STI Program Office, see the following:

- Access the NASA STI Program Home Page at *http://www.sti.nasa.gov*

- E-mail your question via the Internet to help@sti.nasa.gov

- Fax your question to the NASA Access Help Desk at (301) 621-0134

- Telephone the NASA Access Help Desk at (301) 621-0390

- Write to:
  NASA Access Help Desk
  NASA Center for AeroSpace Information
  7121 Standard Drive
  Hanover, MD 21076-1320
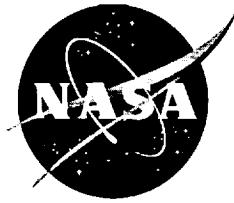
In-Flight Wing Pressure Distributions for the NASA F/A-18A High Alpha Research Vehicle

Mark C. Davis and John A. Saltzman
NASA Dryden Flight Research Center
Edwards, California

Available from the following:

NASA Center for AeroSpace Information (CASI)
7121 Standard Drive
Hanover, MD 21076-1320
(301) 621-0390

National Technical Information Service (NTIS)
5285 Port Royal Road
Springfield, VA 22161-2171
(703) 487-4650

CONTENTS

FIGURES

ABSTRACT

Pressure distributions on the wings of the F/A-18A High Alpha Research Vehicle (HARV) were obtained using both flush-mounted pressure orifices and surface-mounted pressure tubing. During quasi-stabilized 1-g flight, data were gathered at ranges for angle of attack from 5° to 70°, for angle of sideslip from −12° to +12°, and for Mach from 0.23 to 0.64, at various engine settings, and with and without the leading edge extension fence installed. Angle of attack strongly influenced the wing pressure distribution, as demonstrated by a distinct flow separation pattern that occurred between the range from 15° to 30°. Influence by the leading edge extension fence was evident on the inboard wing pressure distribution, but little influence was seen on the outboard portion of the wing. Angle-of-sideslip influence on wing pressure distribution was strongest at low angle of attack. Influence of Mach number was observed in the regions of local supersonic flow, diminishing as angle of attack was increased. Engine throttle setting had little influence on the wing pressure distribution.

INTRODUCTION

Aircraft designers would like to take better advantage of angle of attack and the way it influences the flow about a wing. To help conduct these studies, NASA formed the High Alpha Technology Program (HATP) to improve prediction techniques, provide design guidelines, and investigate new concepts for vortex control on advanced, highly maneuverable aircraft at high angles of attack. The program consisted of wind-tunnel tests of sub-scale and full-scale models and components, calibration for computational fluid dynamics (CFD) codes (ref. 1), piloted simulations, and full-scale flight testing (ref. 2). The full-scale flight test was performed using a modified F/A-18A High Alpha Research Vehicle (HARV), which incorporated thrust-vectoring paddles that allowed sustained, stable flight at high angle of attack. The basic airframe had remained unchanged, so an extensive flowfield and pressure survey study was conducted. The study examined the effects of high angle of attack on the F/A-18A flowfield, and then compared the results with a basic F/A-18A to verify the type of influences that angle of attack had on the flowfield about the aircraft.

The aerodynamics of the F/A-18A HARV were qualitatively documented for the wings, forebody, and leading edge extensions (LEXs) with the use of on-surface and off-surface flow visualization (refs. 3 and 4). Also, pressure data were quantitatively documented on the F/A-18A HARV to understand the vortical flow and lift characteristics of the forebody and the LEX at high angles of attack (ref. 5). The study of the F/A-18A wing configuration at high angle of attack was conducted to better understand the aerodynamic flowfield contributed by the wings.

NOMENCLATURE

a local wing area, in^2

b total wing span, 37.42 ft

c local wing chord, in.

c_l sectional coefficient of lift, $\left[\int (C_{P_{(lower)}} - C_{P_{(upper)}}) d\frac{x}{c} \right] * \cos \alpha$

c_n sectional normal force, $\int (C_{p_{(lower)}} - C_{p_{(upper)}}) d\frac{x}{c}$

C_p static pressure coefficient, $\dfrac{(p - p_\infty)}{\bar{q}_\infty}$

C_p^* pressure coefficient corresponding to local speed of sound,

$$\left(\frac{2}{\Upsilon M_\infty^2}\right)\left\{\left(\frac{(\Upsilon - 1)M_\infty^2 + 2}{\Upsilon + 1}\right)^{3.5}\right\} - 1$$

FS   fuselage station, in.

HARV   High Alpha Research Vehicle

HATP   High Alpha Technology Program

I.D.   inner diameter

LEF   leading-edge flap

LEX   leading-edge extension

M_∞ free-stream Mach number

p static pressure, lb/ft^2

p_∞ free-stream static pressure, lb/ft^2

PCM   pulse code modulation

$\bar{q}_\infty$ free-stream dynamic pressure, lb/ft^2

S total wing area, 400 ft^2

TEF   trailing-edge flap

x distance along wing chord from leading edge, in.

x/c   dimensionless chord length measured from the leading edge

WLS   wings level sideslip

WS   wing station

y distance outboard from aircraft centerline, in.

Symbols

α angle of attack, deg

β angle of sideslip, deg

δ_{LEF} leading-edge flap deflection, deg

δ_{TEF} trailing-edge flap deflection, deg

η semi-span fraction, $2y/b$

Υ specific heat ratio, 1.4

EXPERIMENT DESCRIPTION

The NASA F/A-18A HARV testbed is a thoroughly instrumented aircraft. The following section provides a detailed description of the aircraft, experiment layout, and the conditions for the tests.

Vehicle Description

The NASA F/A-18A HARV (fig. 1), is a single-place aircraft built by McDonnell Douglas (St. Louis, Missouri) and Northrop (Newbury Park, California) Corporations. The aircraft has twin vertical tails canted out 20° from the vertical and differential all-moving horizontal stabilizers. The aircraft is powered by two modified General Electric (Lynn, Massachusetts) F404-GE-400 afterburning turbofan engines. The F/A-18A HARV flies in the fighter escort configuration without stores. The aircraft carries no missiles, and the wingtip missile launch rails have been replaced with wingtip airdata booms. The collective operation of the all-movable horizontal stabilators and the symmetric leading-edge flaps (LEFs) and trailing-edge flaps (TEFs) provided pitch control. Kemple (ref. 6) provided a more detailed description of the F/A-18A HARV.

The aircraft was modified by the addition of externally mounted thrust-vectoring paddles and a spin chute canister. The operating schedule of the flaps was a function of angle of attack and Mach number (M_∞). For $M_\infty \leq 0.76$ and $\alpha \geq 26°$, the deflection of the LEF (δ_{LEF}) is down 33° (maximum), and the deflection of the TEF (δ_{TEF}) is at 0°. The LEXs were mounted on each side of the fuselage from the wing roots to just forward of the windscreen. Figure 2 shows an overview of the vehicle with the experiment in place.

Wing Pressure System

Pressure measurements were made on both the upper and lower surfaces at selected wing stations. These wing station locations correspond closely with orifice locations on the full-scale wind-tunnel model tested in the NASA Ames Research Center 80- by 120-foot (ft) wind tunnel (ref. 7).

Upper and lower surfaces of the left and right wings were instrumented with three chordwise rows of pressure orifices located at an inboard station of wing station (WS) 086 ($\eta = 0.383$), a middle station of WS 129 ($\eta = 0.575$), and an outboard station of WS 191 ($\eta = 0.851$) (fig. 3). The table on the following page shows the number of orifices in each row.

Figure 4 shows a cross-section profile of the F/A-18A wing at WS 086, WS 129, and WS 191. This view displays the wing contours with the LEF, TEF, and aileron in both the undeflected and deflected positions. Flush-mounted pressure taps (fig. 5) were installed internally in the LEF for all three wing stations. At WS 086 and WS 129 (figs. 6 and 7), surface-mounted pressure tubing was used on the upper and lower wing and the TEF. At WS 191, external pressure tubing was used only on the upper and lower wing because of the confined space at the aileron hinge line. To prevent rapid change in the pressure measurement from a step from the installation of the external pressure tubing, the sides of the tubing were

3

faired (ref. 8). The nominal width of the fairing was 1.0 inch (in.) on the wing and 2.0 in. on the TEF. The nominal height of the tubing was 0.125 in. Details about the wing pressure ports are shown in the following table.

Table. Wing station pressure orifice locations for both wings.

WS 086 Upper surface (x/c)	WS 086 Lower surface (x/c)	WS 129 Upper surface (x/c)	WS 129 Lower surface (x/c)	WS 191 Upper surface (x/c)	WS 191 Lower surface (x/c)
0.0000	0.0006	0.000	0.0006	0.000	0.100
0.0006	0.0019	0.0006	0.0017	0.025	0.240
0.0019	0.0038	0.0017	0.0029	0.050	0.300
0.0038	0.0055	0.0029	0.0043	0.100	0.400
0.0055	0.097	0.0043	0.100	0.125	0.500
0.024	0.219	0.025	0.218	0.150	0.600
0.049	0.300	0.050	0.300	0.200	0.622
0.073	0.400	0.075	0.400	0.250	
0.097	0.500	0.100	0.500	0.300	
0.122	0.600	0.125	0.600	0.400	
0.146	0.692	0.150	0.714	0.450	
0.250	0.800	0.250	0.800	0.500	
0.300	0.900	0.300	0.900	0.550	
0.350		0.350		0.600	
0.400		0.400		0.650	
0.450		0.450		0.662	
0.500		0.500			
0.550		0.550			
0.600		0.600			
0.650		0.650			
0.750		0.750			
0.800		0.800			
0.850		0.850			
0.900		0.900			
0.950		0.950			
0.993		0.992			
1.000		1.000			

Instrumentation and Data-Reduction Techniques

Each pressure orifice on the wings was connected to temperature-controlled electronic scanning pressure transducers with pneumatic tubing. The pressure transducers were placed inside the wing as shown in figure 3. The flush-mounted pressure taps on the LEF consisted of 0.050-in. inner diameter (I.D.) stainless-steel tubing. The external flexible tubing aft of the leading-edge flaps had an I.D. of 0.046 in. The tubing length between the pressure port and the pressure transducers had a maximum length of 11 ft at the wing trailing edge. The maximum pneumatic lag of the wing pressure system was estimated to be 0.10 seconds (sec) for an altitude of 30,000 ft (ref. 9).

Reference pressure for the transducers was supplied through 0.25- and 0.062-in. pneumatic tubing to a reference pressure tank with an internal volume of 45 in^3. The reference pressure tank was in a bay on the side of the right inlet, vented through panel holes to the outside, and monitored by a high-resolution absolute pressure transducer (ref. 10). The pressure transducers were scanned sequentially and then recorded at 10 samples per second by a 12-bit pulse code modulation (PCM) data system. In-flight zero differential pressure readings were taken before each test point and were used during postflight data reduction to correct the data for calibration offsets. The differential range of the wing transducers was ±720 lb/ft^2.

Figure 2 (refs. 4 and 11) shows the specially designed airdata probes. On the left wingtip, static pressure and total pressure were measured using a swiveling probe installed 7.3 ft forward of the wingtip leading edge. The swivel probe was designed with four vanes to align the probe head with the local airstream. The swivel probe could align with the local airstream for angle of attack ranging from $-10°$ to $+70°$ and angles of sideslip from $-20°$ to $+20°$. Mach number, altitude, and dynamic pressure were determined using data from the swivel probe on the left wingboom, and were calibrated for free-stream conditions.

Aircraft angle of attack and sideslip were measured by using vanes on the right and left wingtip, and the data were corrected for upwash and sidewash as well as boom bending. Sideslip was determined as the average of the left and right wingboom vane measurements, while angle of attack was measured on the left wingboom and validated on the right wingboom. From published data (ref. 11), angles of attack and sideslip are estimated to be accurate to $\pm1.0°$ for angle of attack up to 70°. Mach is estimated to be accurate to ±0.01 from 0° to 50° angle of attack. Above 50° angle of attack, the Mach accuracy would be either the same or slightly less than the published values.

For the flow visualization flights, tufts were the primary instrumentation used on the right wing (ref. 3). The data for the flow visualization were taken from still photos from the chase aircraft or from onboard video taken from cameras mounted in the wingboom. Oil flow visualization was also performed, but proved inconclusive in the results.

Flight Test Conditions

The data that showed the influence of angle of attack, sideslip, and the presence of the LEX fence on the wing pressure distributions were obtained during quasi-stabilized 1-g flight and while performing slow wings level sideslip (WLS) maneuvers. The range of angle of attack investigated was from 5° to 70°, and sideslip angles ranged from $-12°$ to $+12°$. The altitude range was from 18,000 to 30,000 ft, and

the Mach-number range was from 0.23 to 0.64. These maneuvers were first flown without the LEX fences and then were repeated with the LEX fences.

The data obtained for engine influence on the pressure distribution were gathered at 5° to 15° angle of attack, 0° of sideslip, and target Mach numbers of 0.4 and 0.6. The engine effect data were taken with the LEX fences. The left-hand engine was modulated to maintain the target Mach number while the right-hand engine was put into one of four engine power settings for each of the test points. The engine settings for the tests were off, idle, military, and 85 percent of afterburner power.

Data that show Mach number influence were taken at a Mach-number range of 0.24 to 0.64 at a nominal altitude of 45,000 ft. The angle of attack varied from 20° to 35° with 0° of sideslip. Most of these data were obtained during helix turns, wind-up turns, spiral dives, or during split-S maneuvers. For all of these test points the LEX fences were removed.

DATA UNCERTAINTY

To validate the data in this report, an error analysis was performed. Bias error, precision error, and an uncertainty error analysis were obtained to give an accurate account of how good the data in the report were. The method used is outlined in reference 12.

The uncertainty in coefficient pressure (C_p) is based on the worst-case errors in the measured pressure on the wing, P_∞, and $\bar{q}_\infty$. The errors found in the measured pressure, P_∞, and $\bar{q}_\infty$ do propagate into the uncertainty for the C_p calculation. The data used for this analysis were based on the nominal flight conditions of M = 0.24, at an altitude of 27,000 ft for the whole angle-of-attack range. The typical bias error in P_∞ is ±0.439 lb/ft^2 and in $\bar{q}_\infty$ is ±0.089 lb/ft^2; the worst typical measured pressure error from the electronic scan pressure is ±1.789 lb/ft^2. Calculating precision error and taking into account the bias errors, then, following the equation for propagation error outlined in reference 12, the 95 percent confidence interval for C_p is ±0.05.

RESULTS AND DISCUSSION

This section will discuss the results of the influence of angle of attack on wing pressure, influence of the LEX fence on wing pressure, engine influences on the wing pressure, influences of sideslip on wing pressure, and the influence of Mach number on wing pressure. Each section will state the conditions that the data were gathered under.

Influences of Angle of Attack

The data presented in this section were taken during stabilized 1-g conditions on the F/A-18A HARV without the LEX fence. During maneuvers that exceeded 30° angle of attack, altitude was not held constant. Flow visualization data were obtained on the right wing using both still photography and onboard video. The pressure data were obtained for both the right and left wing. Figure 8 shows summary of the flow visualization results, figure 9 shows the still photos of the tufts, and figures 10 and 11 show the wing pressure distribution results.

6

Figure 8 shows the overall influence of angle of attack on the flow of the wings of the HARV. As seen from the figure, the regions of separated flow grows gradually as angle of attack increases. At $\alpha = 5°$, shown in figures 8(a) and 9(a), the flow on the wing is completely attached. At $\alpha = 15°$, shown in figures 8(b) and 9(b), a small region of separated and disturbed flow can be seen from outboard of WS 129 to just outboard of WS 191, although near the wingtip the flow is still attached. The disturbed flow is where the flow on the wings is on the verge of separation, but is still attached. This attached flow near the wingtip may be caused by wingtip vortices generated by the wingboom. At $\alpha = 20°$, shown in figures 8(c) and 9(c), the separated flow region has grown significantly—stretching from the wingtip inboard to WS 129. Figures 8(d), 8(e), and 8(f) show how the separated regions continue to grow as angle of attack increases. At $\alpha = 60°$, shown in figure 8(f), the entire wing has separated flow.

Figures 10(a) through (c) show how well the right- and left-wing pressures agree with each other. Such agreement is typical for the entire angle-of-attack range flown. To allow ease of comparison, figure 11 shows only the right-wing pressures.

Figure 11(a) shows how angle of attack influences the pressure distribution at WS 086. The most prominent are the leading-edge suction peaks that occur at $\alpha = 10°$ to $30°$, with the largest peak occurring at $25°$ angle of attack. These peaks primarily occur because of accelerated flow around the leading edge. The next prominent feature of the pressure distribution occurs between x/c of 0.1 to 0.3. A suction peak appears just aft of the LEF hinge line that develops at $\alpha = 25°$, and then decreases in strength until disappearing at $\alpha = 35°$. The reason for this second pressure peak may relate to the deflection of the LEF causing the flow to accelerate onto the wing (ref. 13).

The pressure distribution on the lower surface of the wing starts near zero (0.0) at an angle of attack of 5°, and then gradually increases along with angle of attack until 70°, where the pressure distribution is near 1.0, or the maximum pressure coefficient for about 40 percent of the wing. This increase occurs because the flow to the underside of the wing becomes more perpendicular to the surface as the angle of attack increases. As flow on the wing becomes separated, the overall pressure becomes consistent with no significant variations in the pressure curve.

Figure 11(b) shows how angle of attack influences the pressure distribution at WS 129. The pressure distribution along this wing station shares many of the same characteristics seen at WS 086. The large leading-edge suction peak is evident, though at 10° and 15° angle of attack with the largest peak at 15° angle of attack. The secondary pressure peak at WS 086 has not occurred at WS 129, but the other characteristics of the wing pressure distribution are the same although at higher pressure levels when compared with WS 086.

Figure 11(c) shows how angle of attack influences the pressure distribution at WS 191. The pressure distribution along this wing station shares many of the same characteristics seen in both WS 086 and 129. The large leading-edge suction peak is evident, though it occurs at 10° to 25° angle of attack, with the largest peak occurring at 15° angle of attack. The secondary pressure peak at WS 086 but not strongly evident at WS 129 does occur at WS 191. The secondary pressure peak occurs at an angle of attack of 5° at x/c location of 0.25. The peak also occurs at an angle of attack of 10° at x/c of 0.2, indicating that the secondary pressure peak moved forward. The other characteristics of the pressure distribution are similar to WS 086 and WS 129, though at lower levels in comparison.

Figure 12 shows sectional normal force (c_n) as a function of angle of attack. The method of calculating the sectional normal force is outlined in reference 10. The pressure distributions were more

negative inboard than outboard, as seen in figure 11, resulting in higher section normal forces inboard. WS 086 indicates a strong force at the higher angles of attack. WS 129 section normal force is comparable with WS 086 at the lower angles of attack, but levels off as flow becomes separated on the wing. This same trend is true for WS 191 as well, where the section force levels off as flow becomes separated on the wing.

Figure 13 shows the sectional lift for all three wing stations. The section lift calculation is based on coefficient pressure difference between the upper and lower wing, integrated along the chord as a function of angle of attack. As seen in figure 13, the section lift values generated at WS 086 and WS 129 are much higher than that for the section lift at WS 191. The general trend is increasing sectional lift with angle of attack up to where separation disrupts lift. For WS 191, sectional lift stops increasing at $\alpha = 15°$ and begins decreasing at $\alpha = 30°$. For WS 129, sectional lift stops at $\alpha = 20°$ and begins to decrease at $\alpha = 40°$. WS 86 indicates two distinct rises in the lift curve, possibly caused by the LEX vortex, which is delaying the separation on the inboard portion of the wing.

Influences of the LEX Fence

The purpose of the LEX fence was to reduce the strength of the LEX vortex acting on the vertical tails of the F/A-18A (ref. 14). For this section, the data were obtained with no sideslip, having the LEX fence both installed and removed. Figure 14 ((a) and (b)) shows that the pressure distributions on the right and left wing compare well. This agreement is typical for all of the test points flown. To allow ease of comparison, only the right-wing results are shown in the following figures.

Figure 15 presents the wing pressure distributions for the inboard row, mid row, and outboard row, respectively, at an $\alpha = 20°$ with $\delta_{LEF} = 27°$ and $\delta_{TEF} = 8°$. At WS 086, the upper surface wing pressure distribution without the LEX fence indicates a slightly more negative pressure coefficient over most of the chord when compared with the case with the LEX fence. At WS 129, the differences are confined to the leading edge, while there are no significant differences seen at WS 191. For all three rows, the lower surface pressure shows no differences as was expected. This finding remained true for all cases presented in this section.

At $\alpha = 25°$, figure 16 presents wing pressure distributions at $\delta_{LEF} = 33°$ and $\delta_{TEF} = 1°$. Compared with the data at $\alpha = 20°$, the trends are very much the same with the exception of WS 086. With or without the LEX fence, little influence is seen on the suction peak that formed at $x/c = 0.2$, possibly because of a strong LEX vortex.

At $\alpha = 30°$, figure 17 presents the wing pressure distributions with $\delta_{LEF} = 33°$ and $\delta_{TEF} = 0°$. On the inboard row at WS 086, large differences are seen in the pressure distribution. The case with the LEX fence has a smaller pressure peak at the leading edge when compared with the case without the LEX fence. In addition, for the case without the LEX fence a second pressure peak is caused by the LEX vortex right above the LEF (ref. 3). With the LEX fence a more gradual increase is seen in the pressure coefficient. The other two rows show no influence between the two cases.

At $\alpha = 35°$, figure 18 shows the wing pressure distributions with $\delta_{LEF} = 33°$ and $\delta_{TEF} = 0°$. At WS 086 on the LEF, the case without the LEX fence has a higher negative pressure coefficient when compared with the case with the LEX fence; this is caused by the LEX fence weakening the LEX vortex

and its impact on the inboard wing and the LEF. The other two rows show no influence between the two cases.

At $\alpha = 40°$, figure 19 presents the wing pressure distributions with $\delta_{LEF} = 33°$ and $\delta_{TEF} = 0°$. The case without the LEX fence indicates higher suction at all three wing stations, when compared with the case with the LEX fence. This finding shows that without the LEX fence, the LEX vortex still provides lift even though it has burst well forward of the wing (ref. 15). As expected, the effects occur at WS 086, while no differences in pressure coefficient are at WS 191.

At $\alpha = 50°$, figure 20 presents wing pressure distributions with $\delta_{LEF} = 33°$ and $\delta_{TEF} = 0°$. A comparison of the cases with and without the LEX fence shows good agreement, indicating that the LEX fence has little influence at this angle of attack.

At $\alpha = 60°$, figure 21 presents the wing pressure distribution with $\delta_{LEF} = 33°$ and $\delta_{TEF} = 0°$. At this condition, the wing is mostly separated (fig. 8(f)). As expected, the LEX fence influence on the wing pressure distribution is minimal.

Engine Influences on Wing Pressures

The study of engine influences on wing pressure was performed to determine whether any correlation exists between engine throttle settings and the amount of inlet spillage as well as the influence that inlet spillage might have on wing pressure distributions. The effect of engine setting was investigated at two Mach numbers with four different engine settings. The settings investigated were at engine off, idle, maximum military setting, and 85 percent afterburner. The LEX fences were installed for these test points.

Figure 22 shows that at $M_\infty = 0.4$ and $\alpha = 11°$, the only noticeable effect occurs at WS 086. When the engine is off a slight reduction is seen in positive pressure coefficient at the leading edge on the lower surface. At WS 129 and WS 191, there is good agreement of the wing pressure distribution at all engine throttle settings. Only WS 086 and WS 129 has supersonic flow at the leading edge. Figure 23 shows that at $M_\infty = 0.6$ and $\alpha = 5°$, the wing pressure distribution has good agreement at all wing stations at all of the engine settings. The influence of the engine throttle setting is negligible on the wing pressure distributions.

Influence of Sideslip

The data for the sideslip effects were obtained without the LEX fence. The conditions were with $\delta_{LEF} = 33°$, $\delta_{TEF} = 0°$, and the wings were level. The ailerons were positioned to keep the wings level. To accomplish this, the ailerons were constantly changing position. To reflect this constant movement, a table in the figures contains the maximum and minimum position of the ailerons for both the right and left wing.

Sideslip effects at $\alpha = 30°$ are significant as seen in figures 24 to 26. The wing pressure distribution in figure 24 for WS 086 indicates a large difference in pressure distribution between the left and right leading edge. This difference may be accounted for by the flow direction as the maneuver was performed. Aft of $x/c = 0.07$, the wing pressures for both the right and left wing indicate better agreement. Aft of

$x/c = 0.3$, the pressure distribution pattern becomes predictable. Windward flow on the right wing for all three wing stations produces more negative pressure on the upper surface, when compared with leeward flow. For the left wing, the same trend is evident. This trend shows that sideslip does have large influence on the pressure distribution on both the upper and lower surfaces of the wing.

Figures 27 to 29 show that the sideslip effects at $\alpha = 45°$ decrease when compared with $\alpha = 30°$. Figure 27 shows that at WS 086 a small sharp peak appears at the leading edge on the right wing during maximum negative sideslip, but the left wing has a less-pronounced pressure peak at the leading edge. Positive sideslip produces higher negative pressure on the right wing. In figure 28, WS 129 indicates good agreement for the different sideslip cases with some variation in the pressure distribution. Figure 29 shows that at WS 191 at $\alpha = 45°$, little difference is seen in the pressure distribution at the various sideslip angles, so the flow is completely separated at this point. The small pressure difference indicated near the ailerons on the left wing may be caused by the change in the aileron position.

Figures 30 to 32 indicate that at $\alpha = 55°$, sideslip has almost no effect on the wing pressure distribution except for the LEF at WS 086. Figure 30 shows that at WS 086, the maximum negative sideslip produces higher negative pressure on the left LEF, while 0° of sideslip produces a high negative pressure coefficient on the right LEF. Figures 31 and 32, respectively, show that on WS 129 and WS 191, there is very little difference in the pressure distribution, so the flow is completely separated.

Mach Influences on Wing Pressure

Pressure distributions were obtained on the upper and lower wing surfaces at 1-g stabilized flight except for $M_\infty = 0.64$ and $\alpha = 20°$, which was obtained during a wind-up turn maneuver. In figures 33 to 36, chordwise pressure distributions at WS 086, 129, and 191 are presented for an angle-of-attack range from 20° to 35°. In these figures, the Mach numbers are varied from 0.24 to 0.64. Also shown in these figures is the value for sonic flow, Cp^* (refs. 2 and 16) as marked by the dashed line.

Figure 33 shows the effect of Mach on the wing pressures at an $\alpha = 20°$ with $\delta_{LEF} = 27°$, for WS 086, 129, and 191. On WS 086 (figure 33(a)), there is a region of increased suction at Mach 0.64, as compared with Mach 0.30, which begins at the upper LEF hinge line ($x/c \approx 0.17$) and diminishes near $x/c \approx 0.60$. This region is the result of increased flow separation over the upper LEF hinge line. At the wing leading edge, the negative pressure peak is much higher at 0.64 Mach as compared with 0.30 Mach. Supersonic flow is noted at $M_\infty = 0.64$ on the upper LEF between $0.0006 < x/c < 0.073$ and just aft of the upper LEF hinge line ($0.25 < x/c < 0.30$).

Figure 33(b) displays some noticeable differences at WS 129 as compared with WS 0.86. At Mach 0.64, a slight increase in suction originates on the upper surface at $x/c = 0.30$, and slowly increases in magnitude up to $x/c = 0.65$. The region of increased suction at Mach 0.64 occurs farther aft and is smaller in magnitude as compared with the distribution at WS 086. The Mach effects are not known between $0.60 < x/c < 1.0$ because of inactive pressure ports in the chord region at the time of flight test. No noticeable pressure peak appears at the upper leading edge of WS 129 at Mach 0.30 as compared with WS 086. This finding implies that the leading-edge flow separation that was believed to exist at WS 086 and $M_\infty = 0.30$ (fig. 33(a)) does not exist at the corresponding Mach number for WS 129 (fig. 33(b)). Supersonic flow occurs on the entire upper LEF ($0.00 < x/c < 0.15$) at Mach 0.64. At WS 129, a noticeable yet slight increase in pressure appears at the lower leading edge at Mach 0.64, as

10

compared with Mach 0.30. No other noticeable Mach effects were noticed on the lower wing surface at $\alpha = 20°$.

Figure 33(c) shows wing pressure contours at WS 191. The pressure distribution at both Mach numbers is similar in shape, with slightly greater suction on the upper surface at $M_\infty = 0.30$. The flow at Mach 0.64 is supersonic over the entire LEF ($0.00 < x/c < 0.20$). The supersonic region for WS 129, $M_\infty = 0.64$, occupies a larger portion of the LEF as compared with WS 191 at $M_\infty = 0.64$ ($0.00 < x/c < 0.10$). Also, a noticeable region of increased suction appears at Mach 0.30 over the LEF region as compared with $M_\infty = 0.64$, which is common to WS 086 but absent at WS 129. One possible explanation for the presence of separated flow at the leading edge of WS 086 and 191 is the geometric discontinuities that exist upstream of WS 086 and 191. At WS 086, the LEX itself and the LEX fence act as an upstream geometric discontinuity, which could possibly result in leading edge, separated flow and thus a higher suction peak at Mach = 0.30. At WS 191, the air gap at the leading edge from the wing hinge line also acts as an upstream geometric discontinuity and can conversely produce the higher suction peak. Conversely, WS 129 does not have a geometric discontinuity in the near upstream vicinity, which in turn would explain the absence of the increased suction peak at the leading edge.

Figure 34 shows how Mach influenced wing pressures at $\alpha = 25°$ at WS 086, 129, and 191. At WS 086 (fig. 34(a)), the leading-edge suction peaks are similar to those at $\alpha = 20°$, (fig. 33(a)), although the magnitude is slightly reduced. The suction peak is significantly more negative at $M_\infty = 0.20$ than at $M_\infty = 0.64$. There is a rise in suction around $x/c = 0.25$ for both Mach numbers just aft of the LEF hinge line. Slightly higher suction is seen for $M_\infty = 0.64$ (as compared with $M_\infty = 0.29$) aft of the LEF line to the trailing edge. This finding is similar to the $\alpha = 20°$ case; however, the difference is smaller and continues farther aft all the way to $x/c = 1.0$.

Figure 34(b) shows the pressure distribution at WS 129. At $M_\infty = 0.64$, the region of increased suction, as compared with Mach = 0.30, on the upper surface originates farther aft ($x/c = 0.35$) as compared with $\alpha = 20°$ ($x/c = 0.30$), and continues at a constant increase to $x/c = 0.60$. Between $0.0 < x/c < 0.35$, there is more suction at Mach = 0.29 as compared with $M_\infty = 0.64$. No noticeable pressure peak is seen at the wing leading edge at either Mach number. As previously described for figure 33(b), this too is most likely because of separated flow. The flow is supersonic over the same upper surface x/c region at $M_\infty = 0.64$ and $\alpha = 25°$ as compared with $\alpha = 20°$ at WS 129. A noticeable yet slight increase in pressure is seen at the lower leading edge at $M_\infty = 0.64$ for WS 129 as compared with $M_\infty = 0.29$ for WS 129. No other noticeable Mach effects are noticed on the lower wing surface at $\alpha = 25°$.

Figure 34(c) shows the pressure distribution at WS 191. The pressure distribution pattern is similar to that for $\alpha = 20°$ at WS 191. The flow is supersonic over the same upper wing x/c region at $M_\infty = 0.64$ and $\alpha = 25°$, as compared with $M_\infty = 0.64$ and $\alpha = 20°$. The supersonic region for WS 129 at $M_\infty = 0.60$ occupies a smaller portion of the LEF, as compared with WS 191 at $M_\infty = 0.60$. The pressure peak at the upper leading edge identified at $\alpha = 20°$ and $M_\infty = 0.30$ is substantially reduced at $\alpha = 25°$ and $M_\infty = 0.29$. However, the argument that explains the presence of the suction peak at WS 086 and 191 ($M_\infty = 0.30$ and $\alpha = 20°$) with the absence of the pressure peak at WS 129 applies here also ($M_\infty = 0.29$ and $\alpha = 25°$).

As shown in figure 34 ($\alpha = 25°$), WS 086 is significantly affected by Mach whereas such effects are noticeably less significant at WS 129 and 191. The overall Mach effects at all wing stations is noticeably lower at $\alpha = 25°$ as compared with $\alpha = 20°$.

Figure 35 shows the effects of Mach on wing pressures at $\alpha = 30°$ at WS 086, 129, and 191. As shown in figure 35(a) ($M_\infty = 0.60$), Mach has little influence on the pressures aft of $x/c = 0.25$. The Mach 0.26 upper surface suction region is noticeably higher than the Mach-0.60 distribution between $0.00 < x/c < 0.10$. A large pressure peak is still near the leading edge at $M_\infty = 0.26$. Supersonic flow is noted for $M_\infty = 0.64$ between $0.00 < x/c < 0.024$ and at $x/c = 0.25$.

The upper and lower surface pressure distributions at WS 129 (fig. 35(b)) are equivalent for $M_\infty = 0.26$ and 0.60 except for the LEF. A slight increase is seen in suction on the upper LEF at $M_\infty = 0.60$ between $0.00 < x/c < 0.15$ as compared with $M_\infty = 0.26$. A slight increase is also seen in pressure at the lower leading edge at $M_\infty = 0.60$ for WS 129 as compared with $M_\infty = 0.26$ for WS 129. No other noticeable Mach effects is noticed on the lower wing surface at $\alpha = 30°$. The supersonic region on the upper LEF at $\alpha = 30°$ and $M_\infty = 0.60$ occurs between $0.00 < x/c < 0.15$. The magnitude of the supersonic flow on the upper LEF is lower in magnitude at $\alpha = 30°$ for WS 129 as compared with $\alpha = 30°$ for WS 086.

As shown in figure 35(c), no significant Mach effects at WS 191 are seen except for increased suction at the leading edge for the $M_\infty = 0.60$ at $\alpha = 30°$ condition. Supersonic flow occurs only at the leading edge of WS 191 for Mach 0.60.

As shown in figure 35, at $\alpha = 30°$, the leading edge region of WS 086 is significantly affected by Mach whereas Mach only had a minor effects at WS 129 and 191. The overall Mach effects at all wing stations are noticeably lower at $\alpha = 30°$ as compared with $\alpha = 25°$.

Figure 36 shows the effects of Mach on wing pressures at an $\alpha = 35°$, for WS 086, 129, and 191. As shown in figure 36(a), a slight increase in suction is seen on the forward portion of the upper LEF $(0.00 < x/c < 0.10)$ for WS 086 at Mach 0.54.

The upper surface of WS 129 (fig. 36(b)) shows no significant Mach effects between Mach 0.54 and 0.24. A noticeable yet slight increase in pressure is seen at the lower leading edge at Mach 0.54 for WS 129 as compared with Mach 0.24.

No other noticeable Mach effects are seen on the upper or lower wing surface at $\alpha = 35°$ in figure 36. Supersonic flow is noticed on the upper LEF for WS 086 at Mach 0.54 between $0.00 < x/c < 0.15$. The flow in the rest of the wing was subsonic at all wing stations.

Upon review of figures 33 to 36, the upper surface wing areas occupied by supersonic flow appears to move inboard as angle of attack increases from 20° to 35°.

As shown in figure 36, at $\alpha = 35°$, there is evidence of a minor Mach effect at the upper leading edge region between $0.00 < x/c < 0.10$ at WS 086. Mach effects on the rest of the wing surface are minimal.

CONCLUDING REMARKS

Pressure distributions were obtained at three wing stations on the F/A-18A HARV. The data were gathered at various angles of attack and sideslip, engine throttle settings, and Mach numbers, and with and without a LEX fence installed. The angle-of-attack range was 5° to 70°, the angle-of-sideslip range

was from –12° to +12°, the Mach-number range was from 0.23 to 0.64, and the altitude range was 18,000 to 30,000 ft.

Angle of attack influenced the upper surface of the wings by changing the magnitude of the suction peak at the leading edge and the separation pattern on the wing. Separation of flow on the upper surface began at about 15° angle of attack. The area of upper surface separated flow increased with angle of attack up to $\alpha = 60°$. On the lower surface, the pressure distribution increase in magnitude was proportional to the increase in angle of attack.

The LEX fence influenced upper surface pressure distributions by changing the LEX vortex on the inboard portion of the wing from an angle of attack from 30° to 40°, with a little influence at 60°.

Sideslip did affect wing pressure distribution, indicated by the increase in suction on the upper surface of the wing during the sideslip maneuvers to the windward side. Angle of sideslip affected the strength and placement of attached flow on the wing. Sideslip effects near the trailing edge of the wing at WS 191 were obscured by aileron effects.

Influence of Mach number on the wing pressure distributions decreased as angle of attack increased from $\alpha = 20°$ to 35°. The upper surface wing areas occupied by supersonic flow appeared to decrease in magnitude and move inboard as angle of attack increased from 20° to 35°. The outer wing station indicated the least influence by Mach number, while the inner wing station had the greatest influence by Mach number.

Varying the engine throttle setting on the F/A-18A had minimal effect on wing pressure distribution.

Dryden Flight Research Center
National Aeronautics and Space Administration
Edwards, California, November 26, 1999

REFERENCES

1. Thomas, James L., Robert W. Walters, Taekyu Reu, Farhad Ghaffari, Robert P. Weston, and James M. Luckring, "A Patched-Grid Algorithm for Complex Configurations Directed Towards the F/A-18 Aircraft," AIAA-89-0121, January 1989.

2. Fisher, David F., Daniel W. Banks, and David M. Richwine, *F-18 High Alpha Research Vehicle Surface Pressures: Initial In-Flight Results and Correlation With Flow Visualization and Wind-Tunnel Data*, NASA TM-101724, August 1990.

3. Fisher, David F., John H. Del Frate, and David M. Richwine, *In-Flight Flow Visualization Characteristics of the NASA F-18 High Alpha Research Vehicle at High Angles of Attack*, NASA TM-4193, May 1990.

4. Fisher, David F., David M. Richwine, and Daniel W. Banks, *Surface Flow Visualization of Separated Flows on the Forebody of an F-18 Aircraft and Wind-Tunnel Model*, NASA TM-100436, May 1988.

5. Richwine, David M. and David F. Fisher, *In-Flight Leading-Edge Extension Vortex Flow-Field Survey Measurements on a F-18 Aircraft at High Angle of Attack*, NASA TM-4398, September 1992.

6. Kemple, Robert W., *F-18 HARV High Alpha Research Vehicle Description*, NASA CR-186029, March 1994.

7. Fisher, David F. and Wendy R. Lanser, "Flight and Full-Scale Wind-Tunnel Comparison of F/A-18 Pressure Distributions from an F-18 Aircraft at High Angles of Attack," *Fourth NASA High Alpha Conference*, NASA Conference Publication 10143, vol. 1, paper no. 2, July 1994.

8. Montoya, Lawrence C. and David P. Lux, *Comparisons of Wing Pressure Distribution From Flight Tests of Flush and External Orifices for Mach Numbers From 0.50 to 0.97*, NASA TM X-56032, April 1975.

9. Lamb, J. P., Jr., *The Influence of Geometry Parameters Upon Lag Error in Airborne Pressure Measuring Systems*, WADC TR 57-351, July 1957.

10. Saltzman, Edwin J., John H. Del Frate, Catherine M. Sabsay, and Jill M. Yarger, *Pressure Distribution for the Wing of the YAV-8B Airplane; With and Without Pylons*, NASA TM-4429, November 1992.

11. Moes, Timothy R. and Stephen A. Whitmore, *A Preliminary Look at Techniques Used to Obtain Airdata From Flight at High Angles of Attack*, NASA TM-101729, Dec. 1990.

12. Coleman, Hugh W. and W. Glenn Steele, Jr., *Experimentation and Uncertainty Analysis for Engineers*, John Wiley & Sons, New York, New York, 1989.

13. Rose, Leonard M. and John M. Altman, *Low-Speed Investigation of the Stalling of a Thin, Faired, Double-Wedge Airfoil With Nose Flap*, NACA TN-2172, August 1950.

14

14. Erikson, G. E., R. M. Hall, D. W. Banks, J. H. Del Frate, J. A. Schreiner, R. J. Hanley, and C. T. Pulley, "Experimental Investigation of the F/A-18A Vortex Flows at Subsonic Through Transonic Speeds, Invited Paper," AIAA-89-2222, 1989.

15. Del Frate, John H. and Fanny A. Zuniga, "In-Flight Flow Field Analysis on the F-18 High Alpha Research Vehicle With Comparisons to Ground Facility Data," AIAA-90-0231, January 1990.

16. Whitmore, Stephen A. and Timothy R. Moes, *The Effects of Pressure Sensor Acoustics on Airdata Derived From a High-Angle-of-Attack Flush Airdata Sensing (HI-FADS) System*, NASA TM-101736, February 1991.
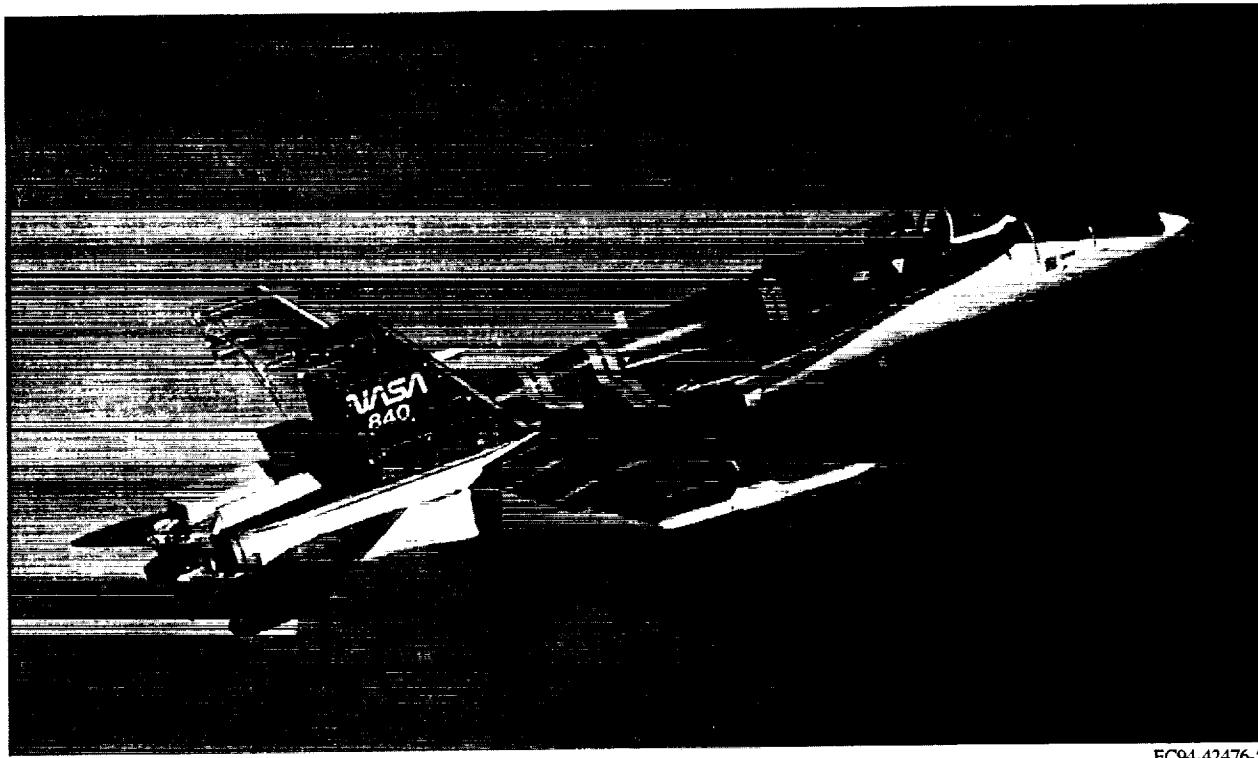
EC94-42476-5

Figure 1. NASA F/A-18A HARV.
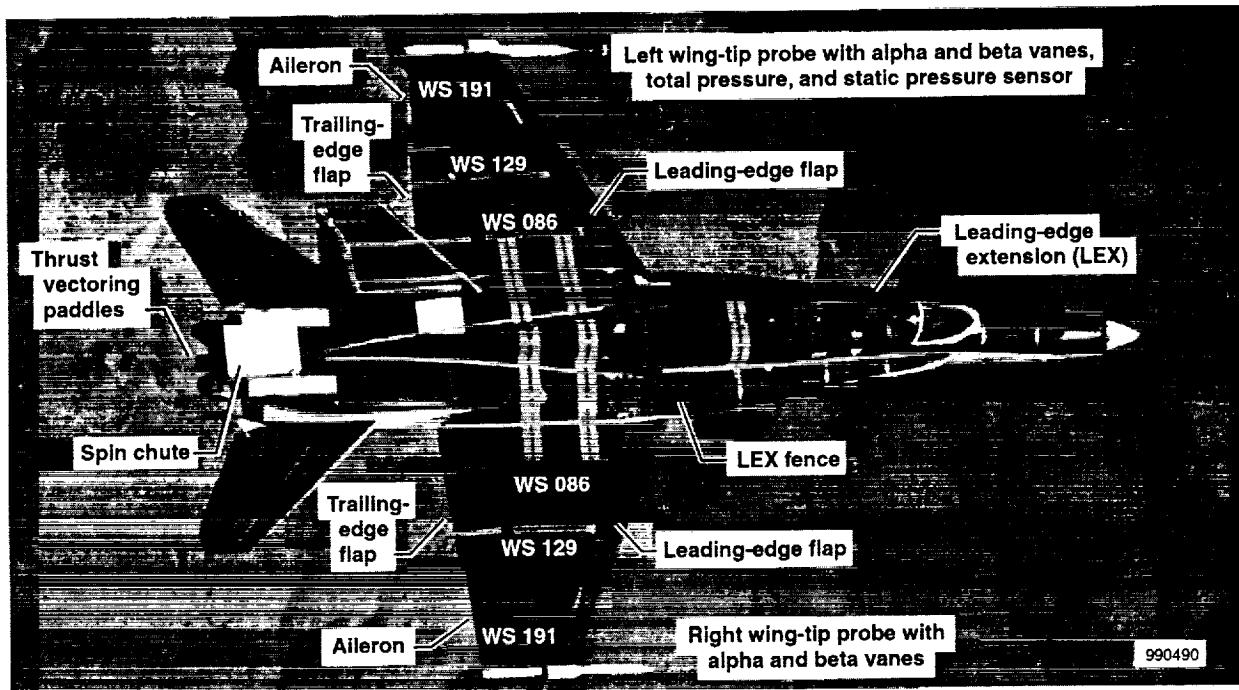
Figure 2. Wing pressure experiment on the F/A-18A HARV.
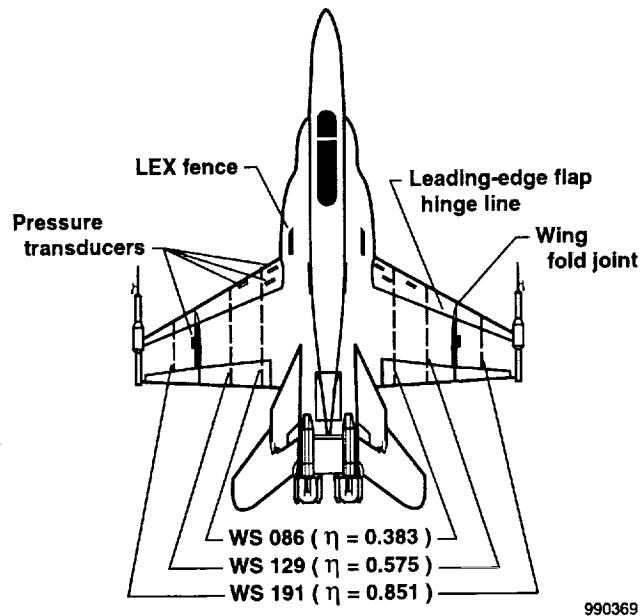
Figure 3. Location of wing pressure rows and pressure modules.
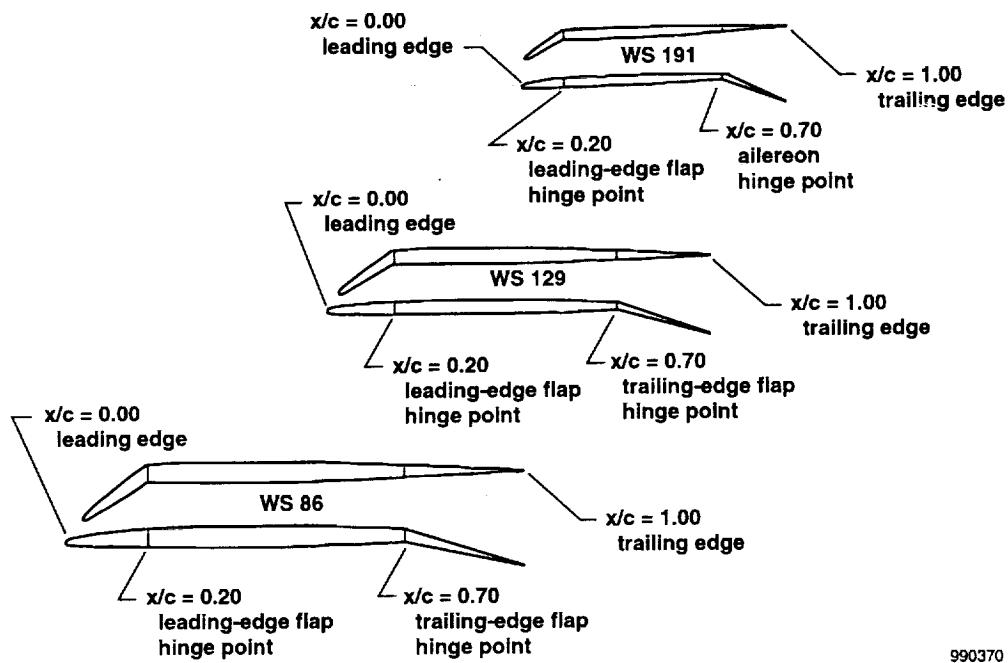
Figure 4. Wing profiles with flaps in deflected and undeflected positions.
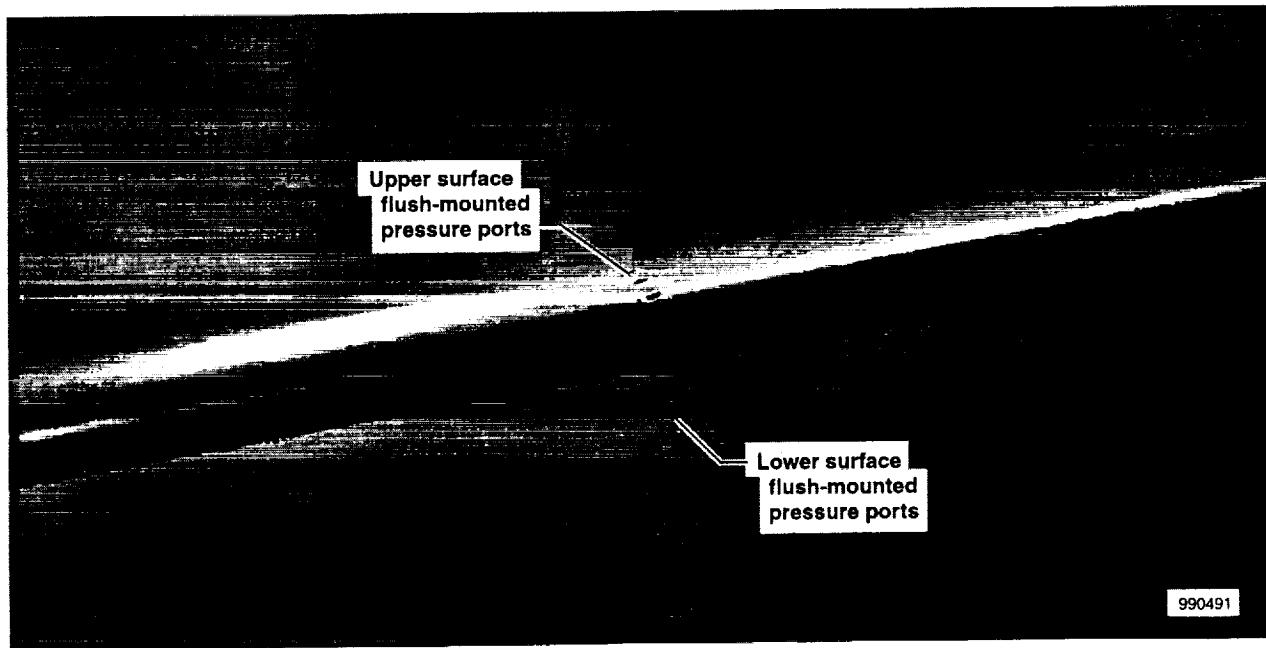
Figure 5. Flush-mounted pressure ports located on LEF.
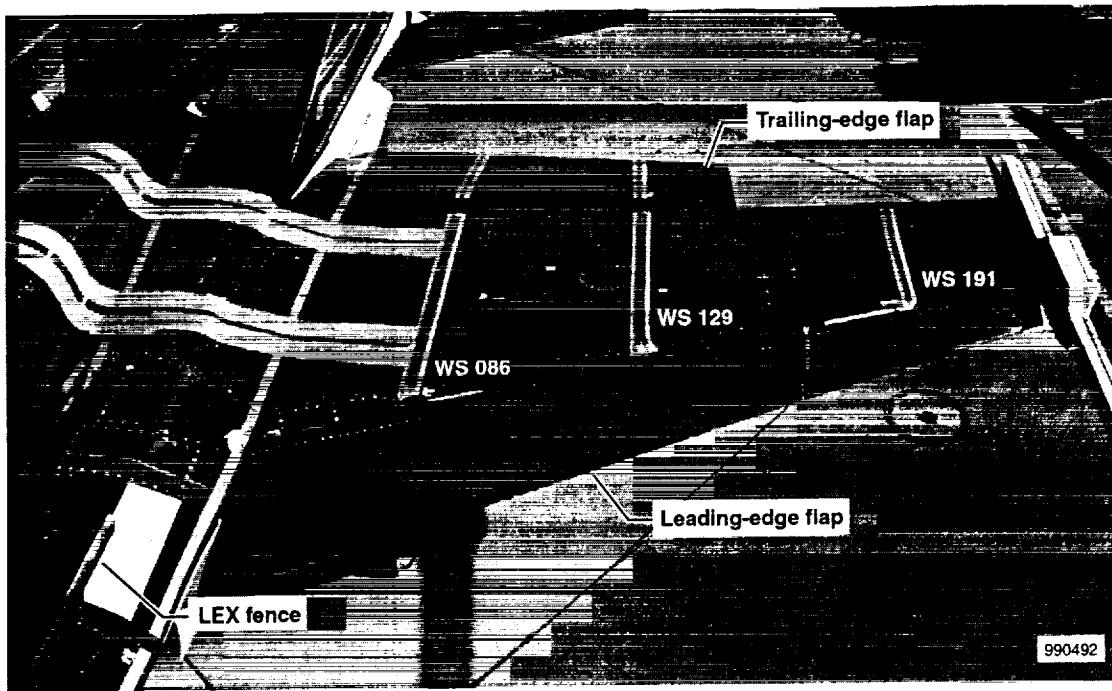
Figure 6. Pressure row configuration, upper left wing, looking aft.

18
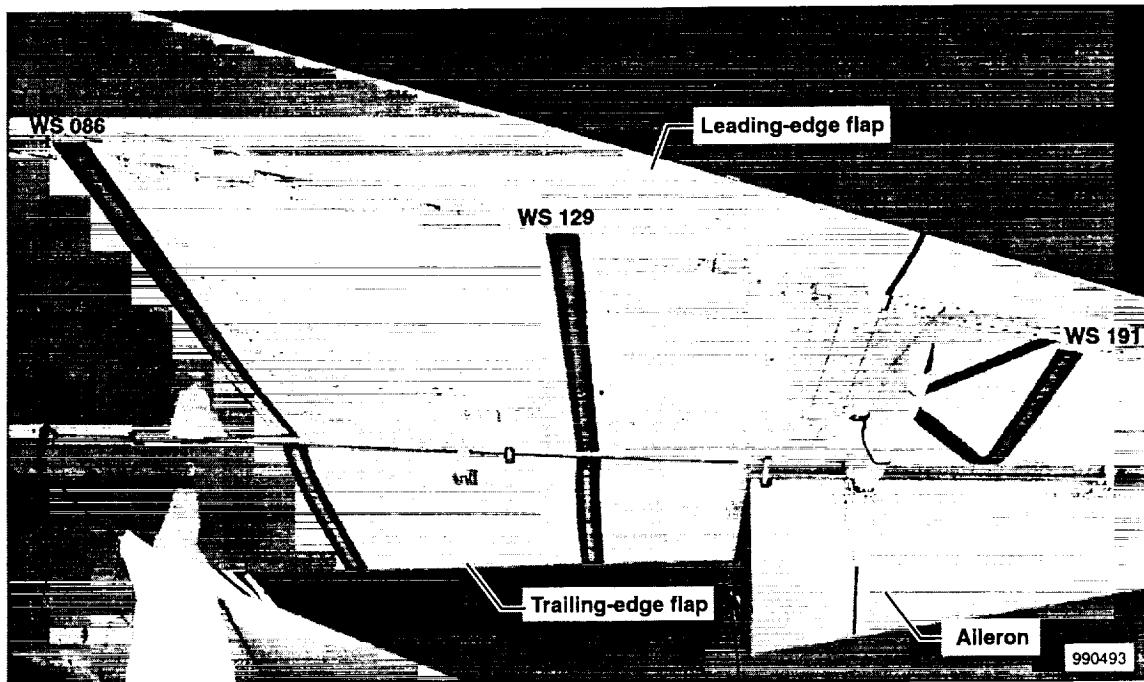
Figure 7. Pressure row configuration, lower left wing, looking aft.
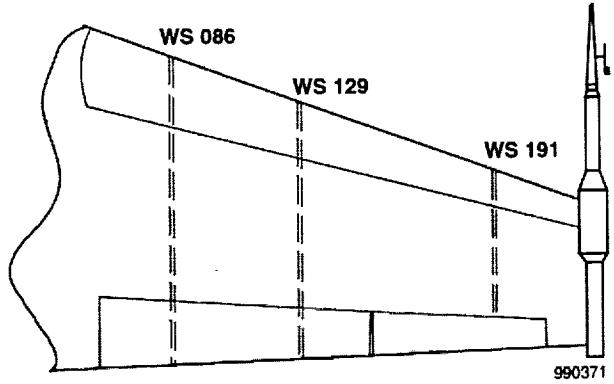
(a) $\alpha = 5°$.
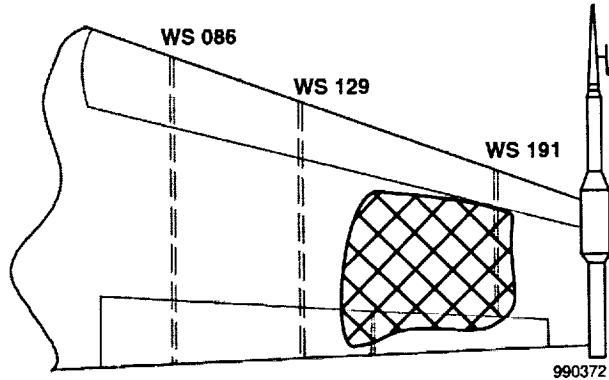
(b) $\alpha = 15°$.
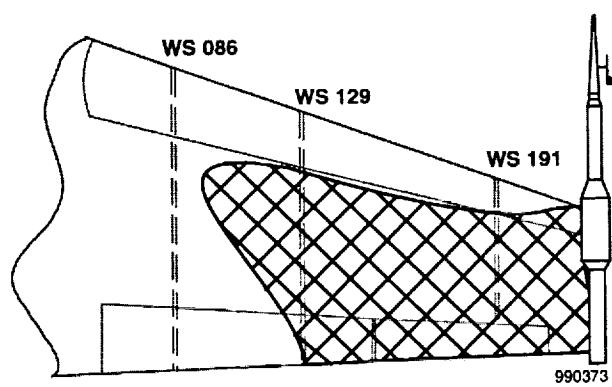
(c) $\alpha = 20°$.
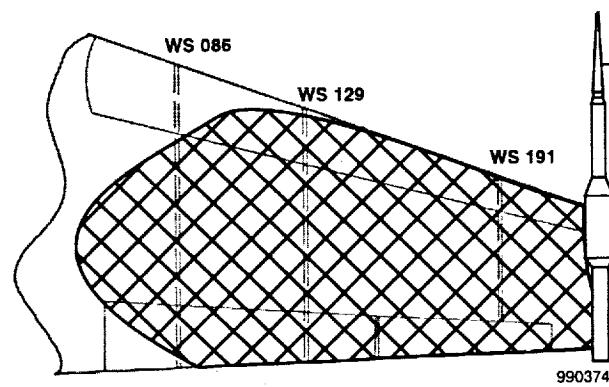
(d) $\alpha = 30°$.
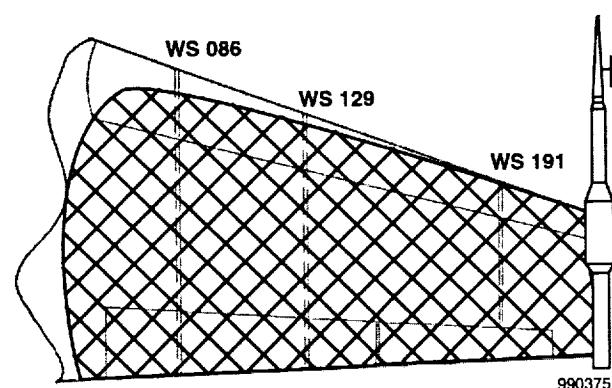
(e) $\alpha = 40°$.
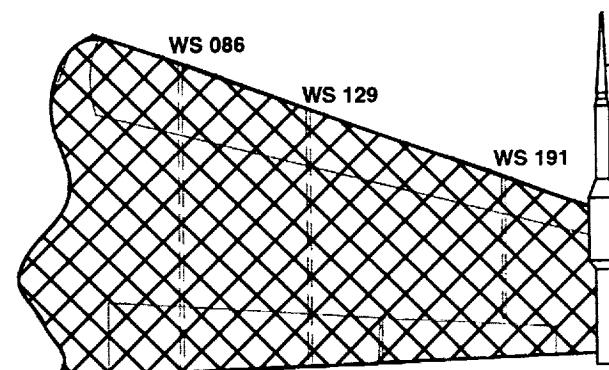
(f) $\alpha = 60°$.

Figure 8. Separation pattern on the upper surface of the wing as a function of angle of attack.

20
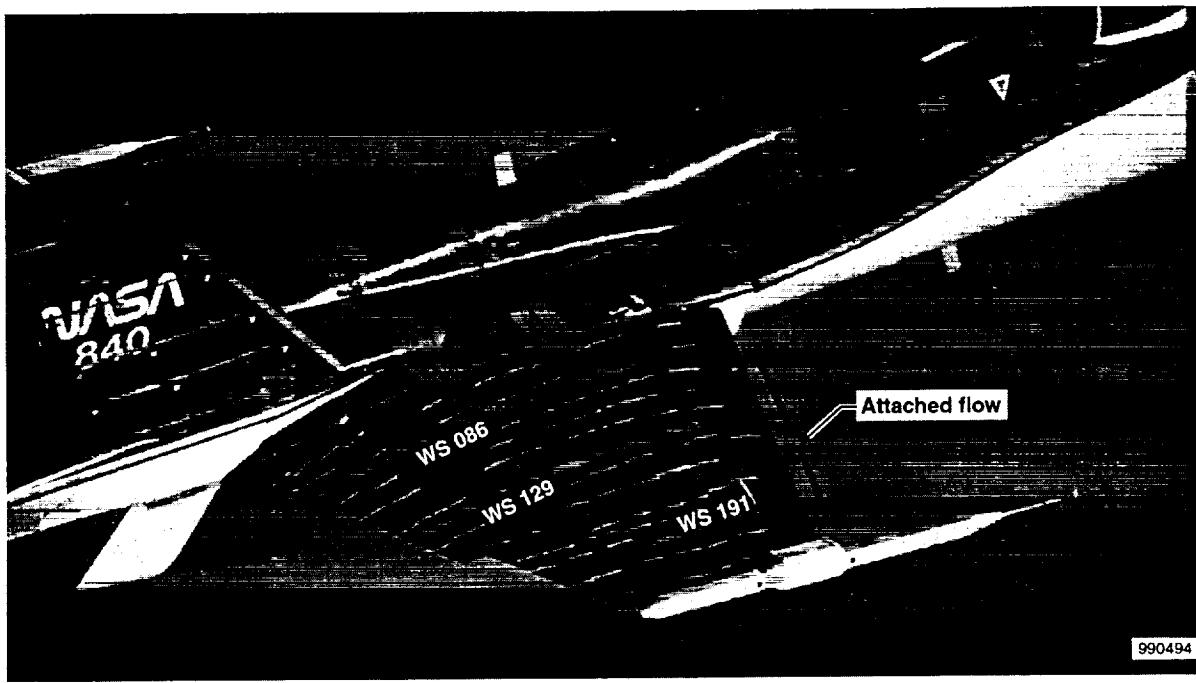
(a) $\alpha = 5°$.
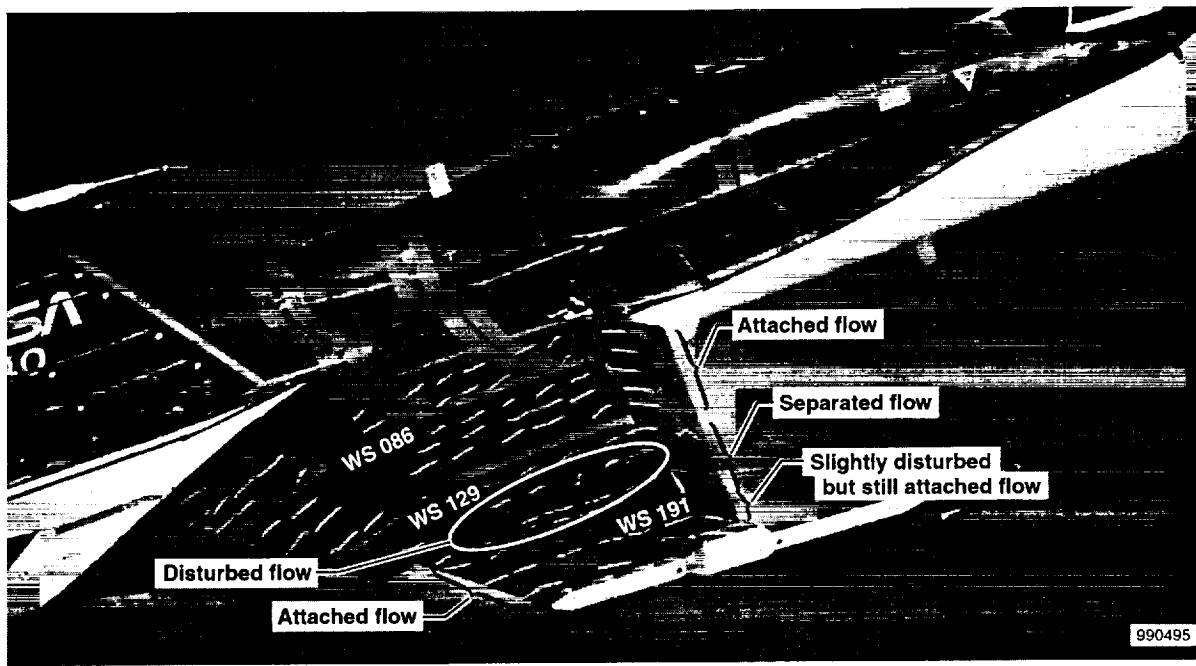
(b) $\alpha = 15°$.

Figure 9. Flow visualizations with tufts.
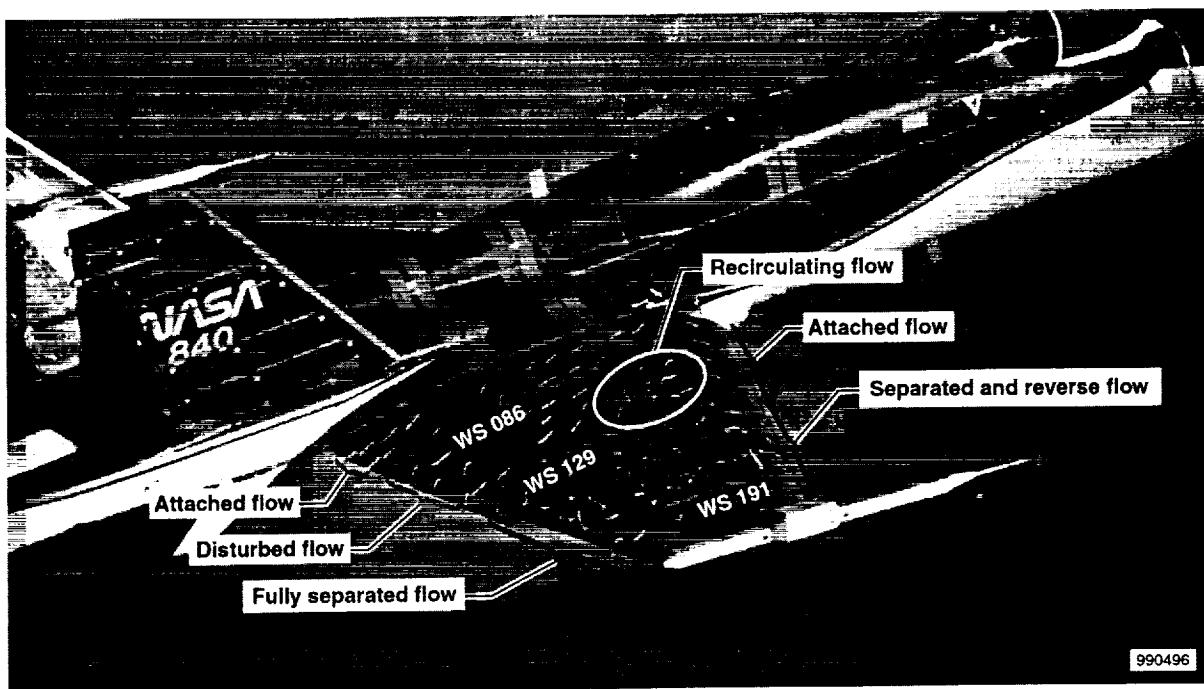
9(c) $\alpha = 20°$.

Figure 9. Concluded.
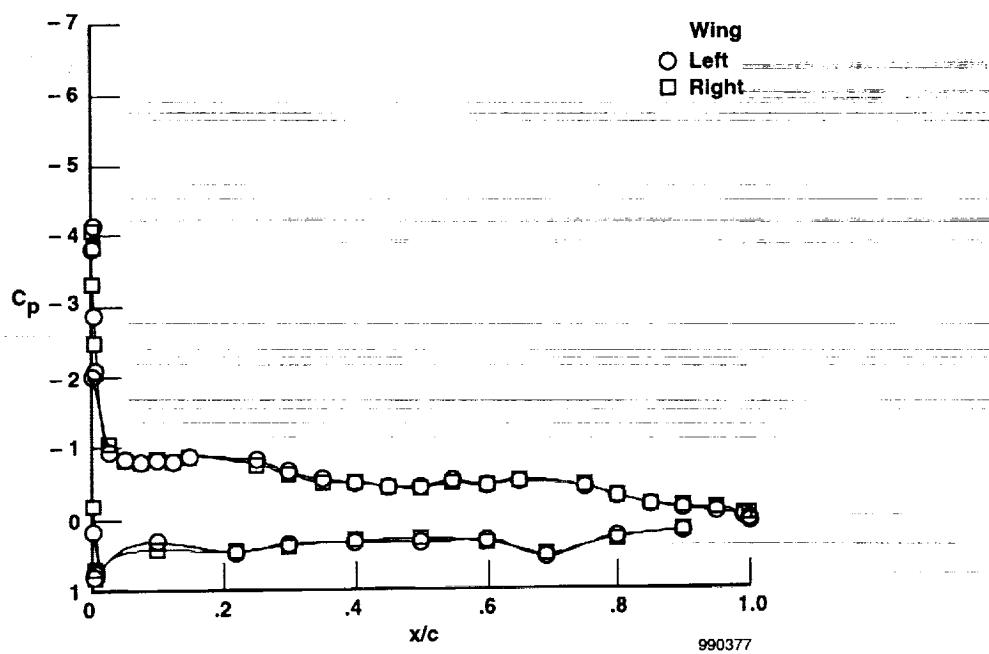
(a) WS 086.

Figure 10. Wing pressure distribution with $\alpha = 10°$, $\beta = 0.0°$, $\delta_{LEF} = 27°$, $\delta_{TEF} = 8°$.
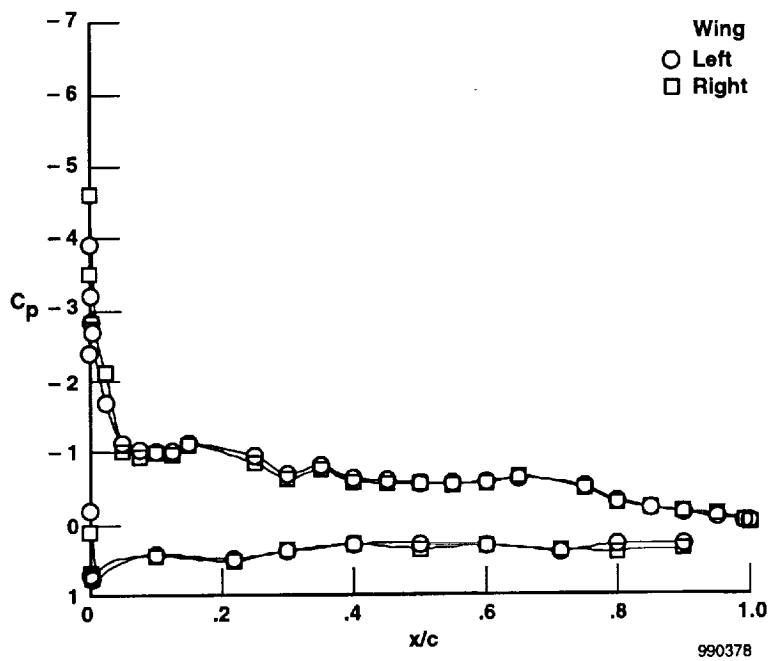
(b) WS 129.
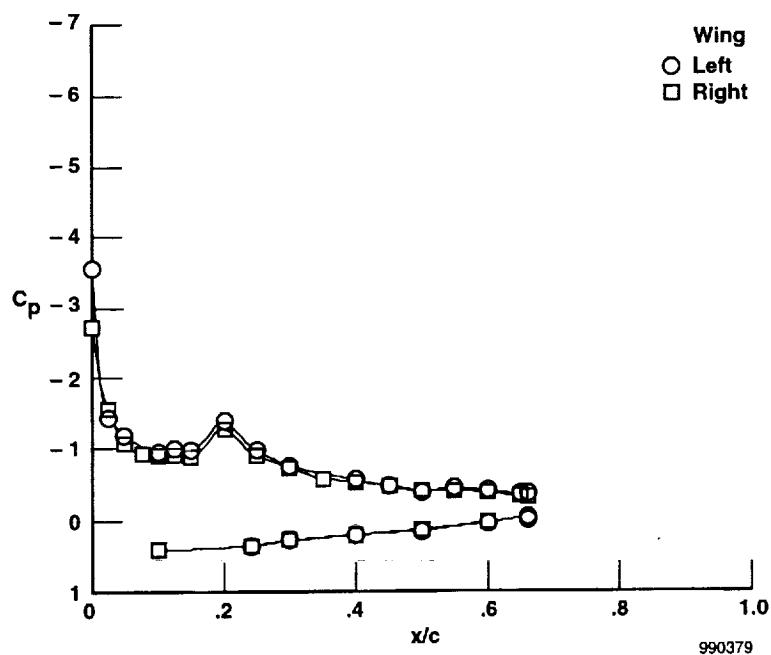
(c) WS 191.

Figure 10. Concluded.
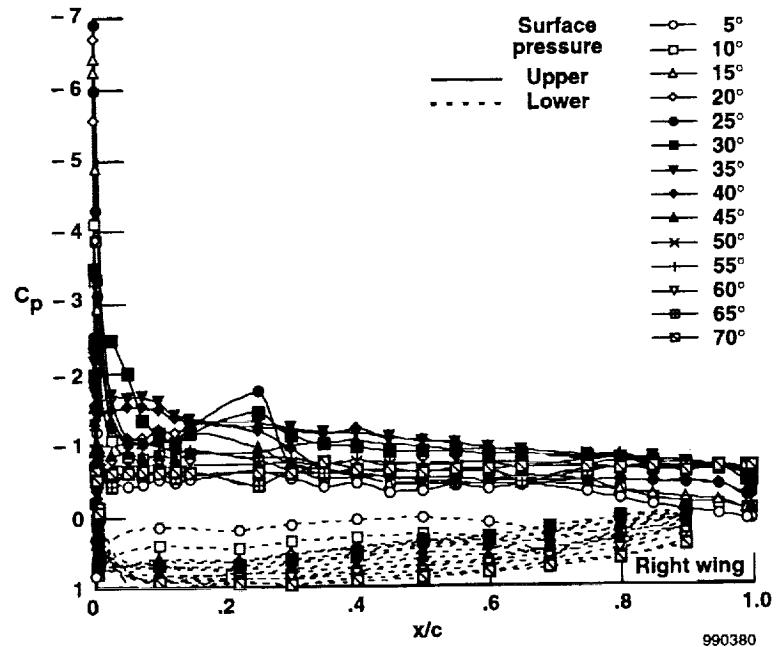
(a) WS 086.
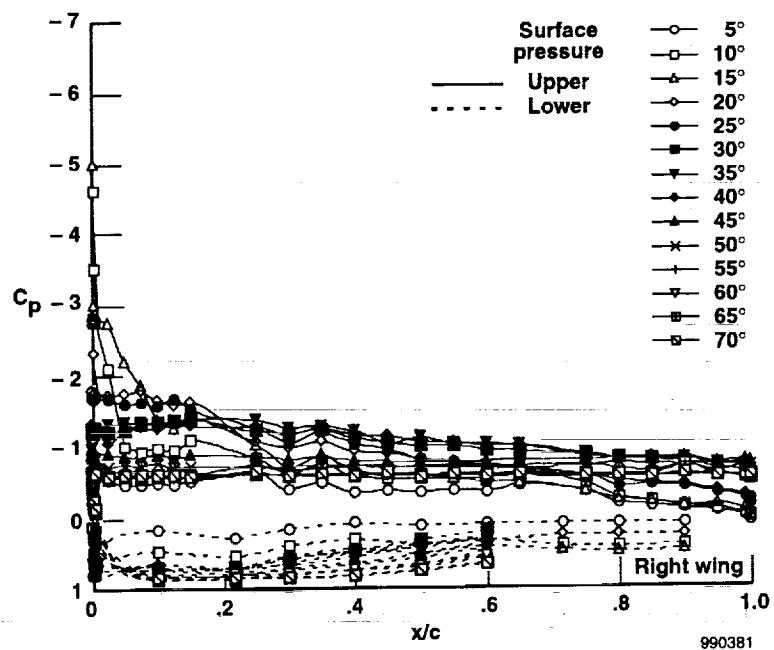
(b) WS 129.

Figure 11. Wing pressure distributions.

24
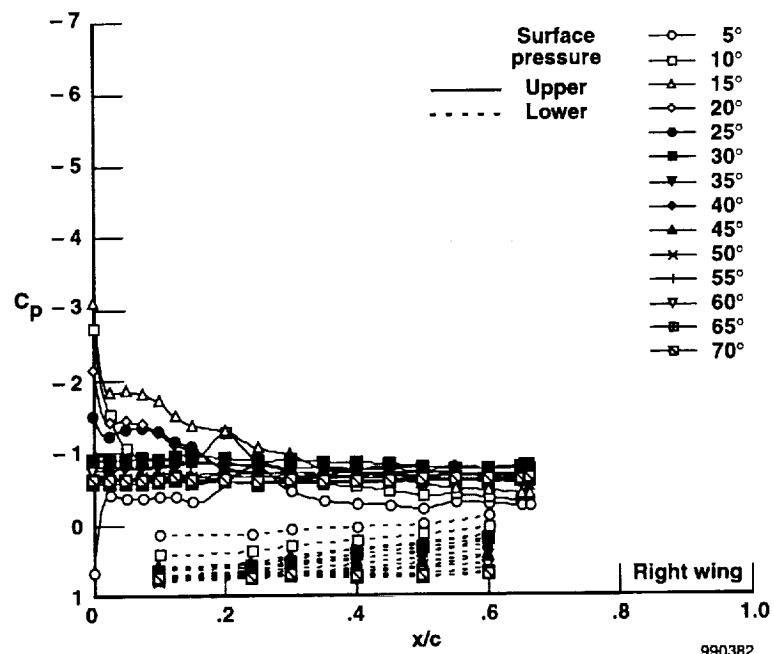
(c) WS 191.

Figure 11. Concluded.
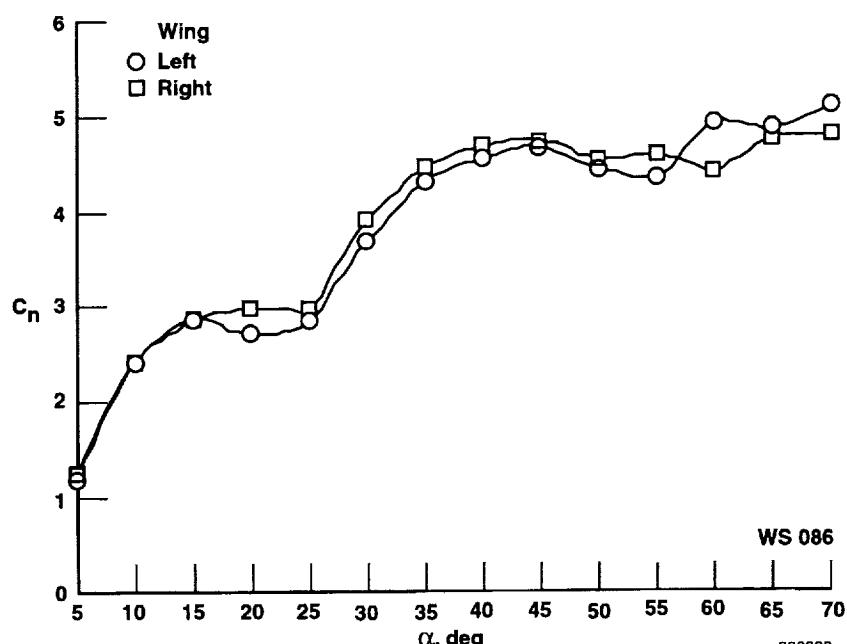
(a) WS 086.

Figure 12. Sectional normal force (c_n) as a function of angle of attack.

25
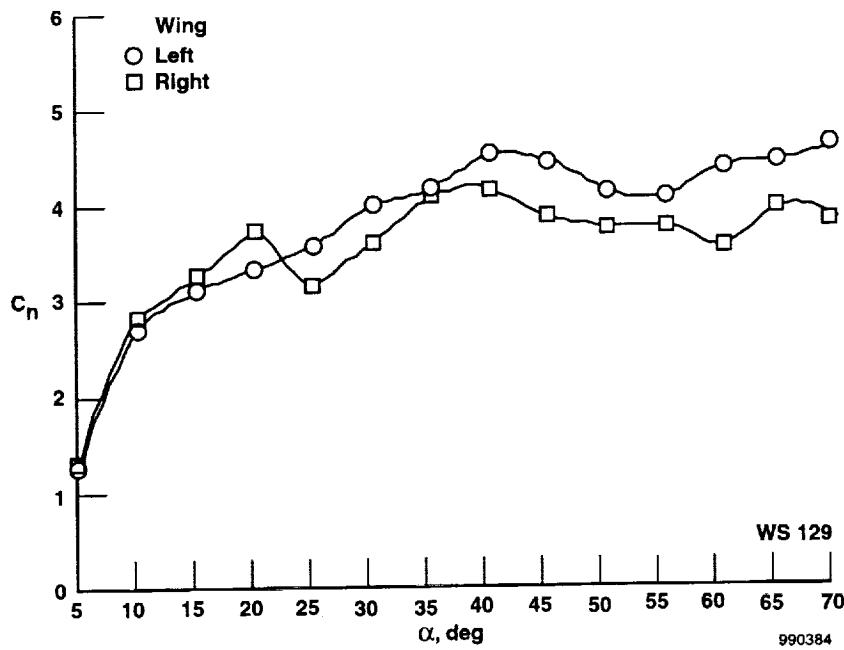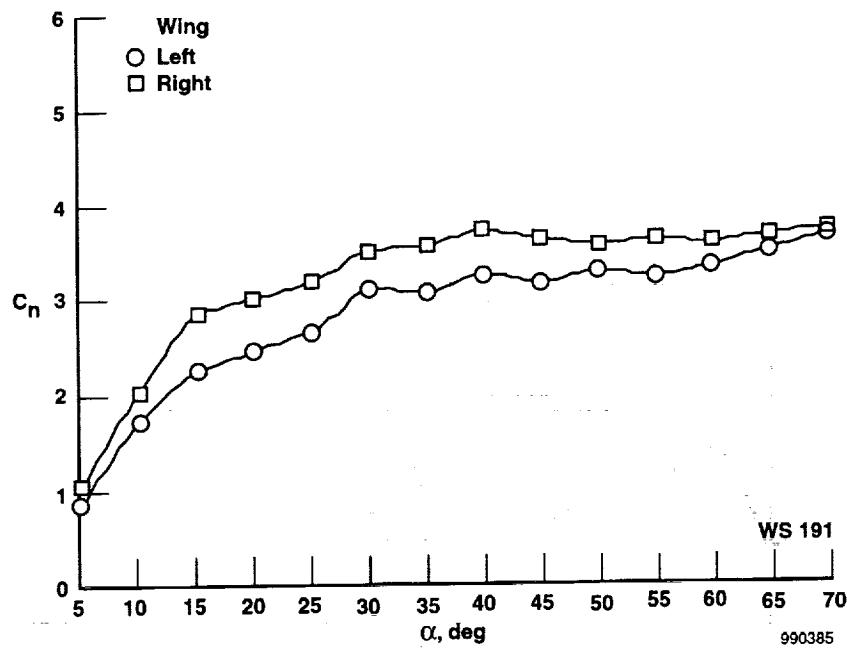
(b) WS 129.

(c) WS 191.

Figure 12. Concluded.

26
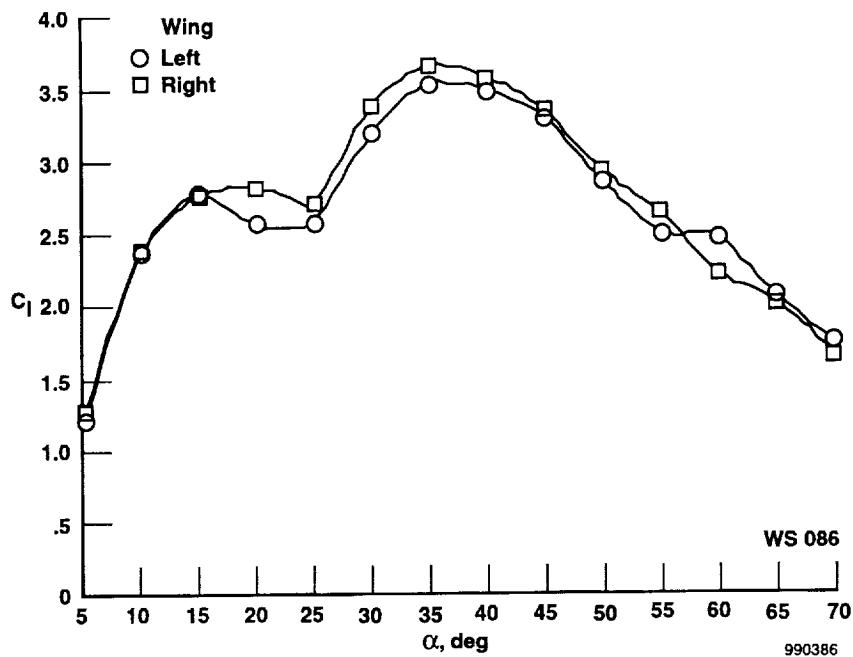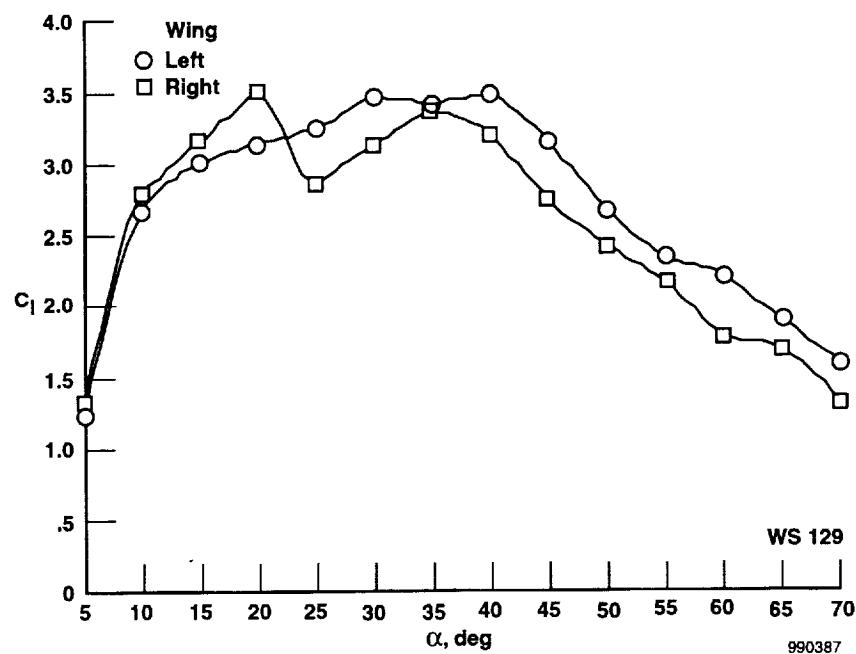
(a) WS 086.

(b) WS 129.

Figure 13. Section lift force as a function of angle of attack.

27
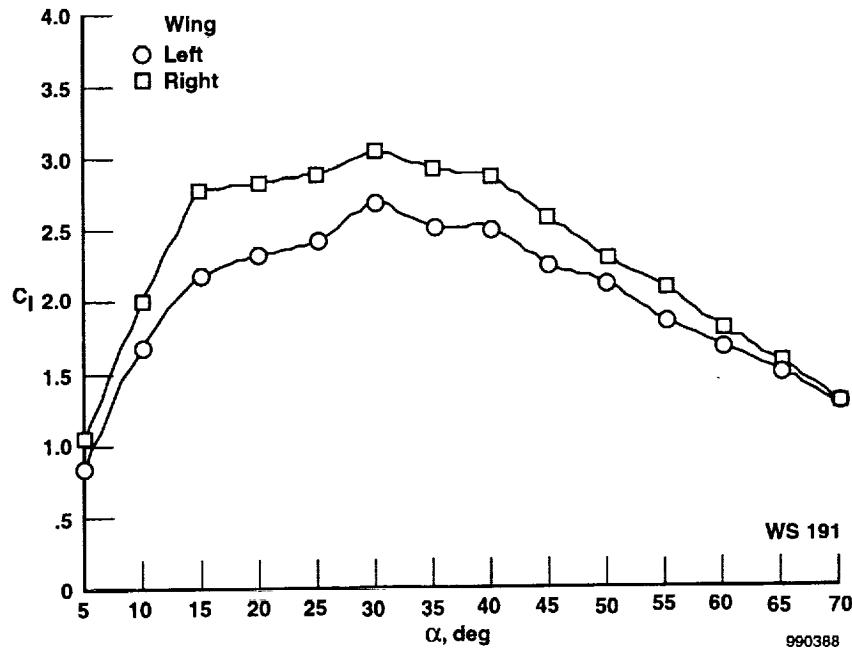
(c) WS 191.

Figure 13. Concluded.
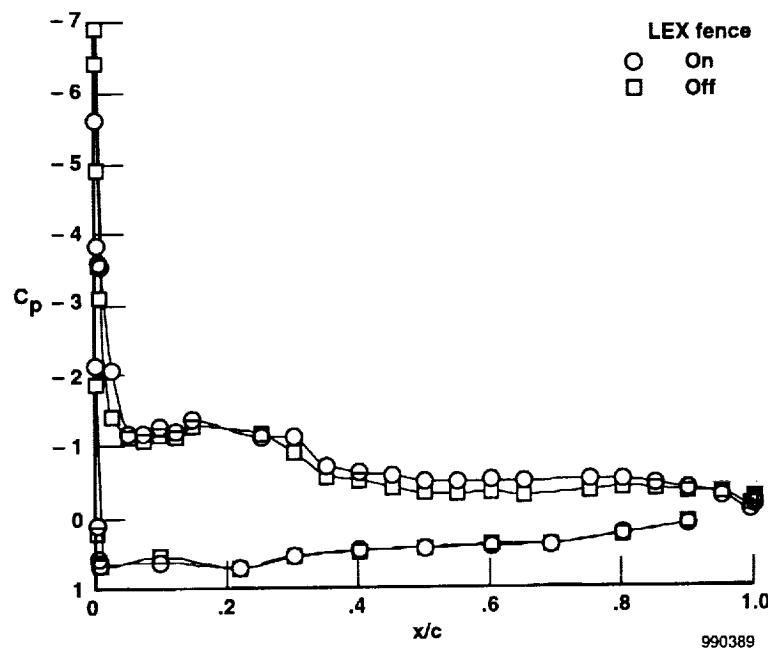
(a) Right wing.

Figure 14. LEX fence effects with $\alpha = 20°$, $\beta = 0°$, $M_\infty = 0.3$, $\delta_{LEF} = 27°$, $\delta_{TEF} = 8°$.
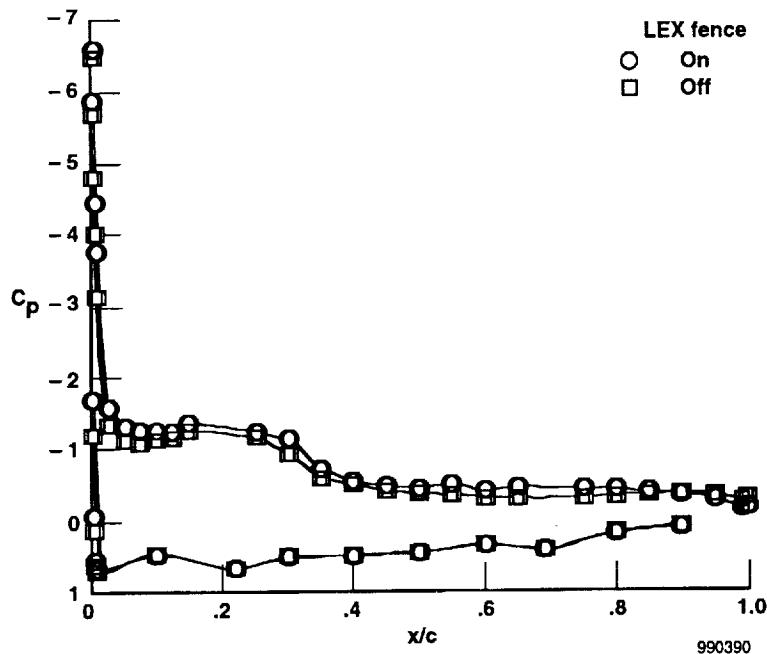
(b) Left wing.

Figure 14. Concluded.
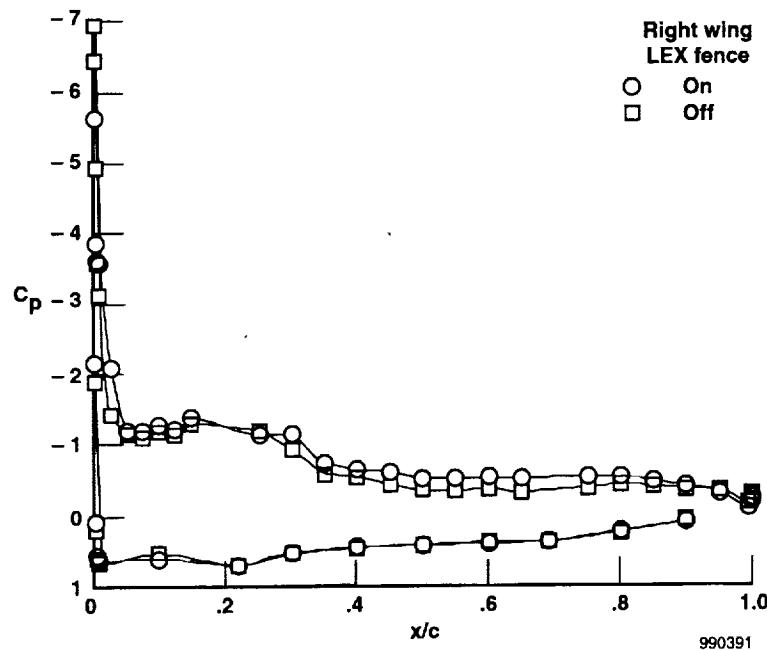
(a) WS 086.

Figure 15. LEX fence effects with $\alpha = 20°$, $\beta = 0°$, $M_\infty = 0.3$, $\delta_{LEF} = 27°$, $\delta_{TEF} = 8°$.
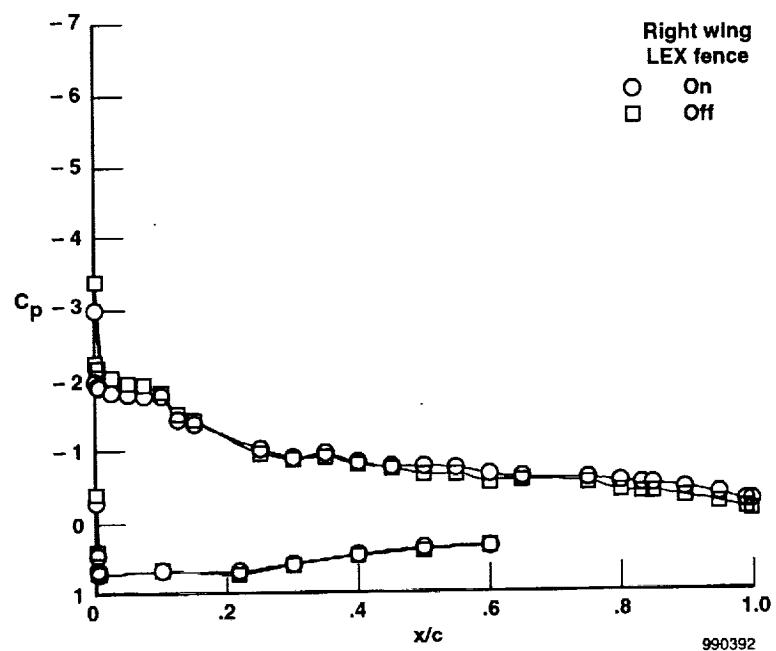
(b) WS 129.
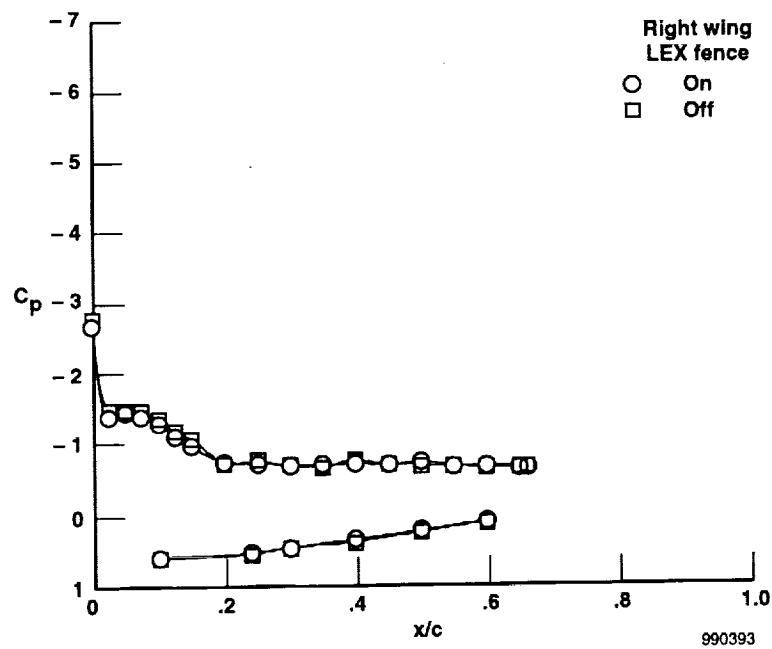
(c) WS 191.

Figure 15. Concluded.
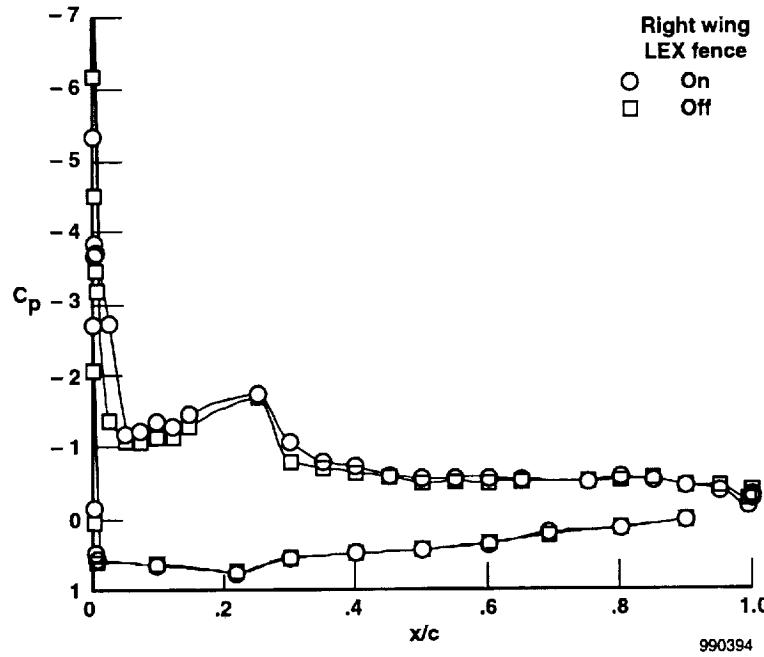
(a) WS 086.
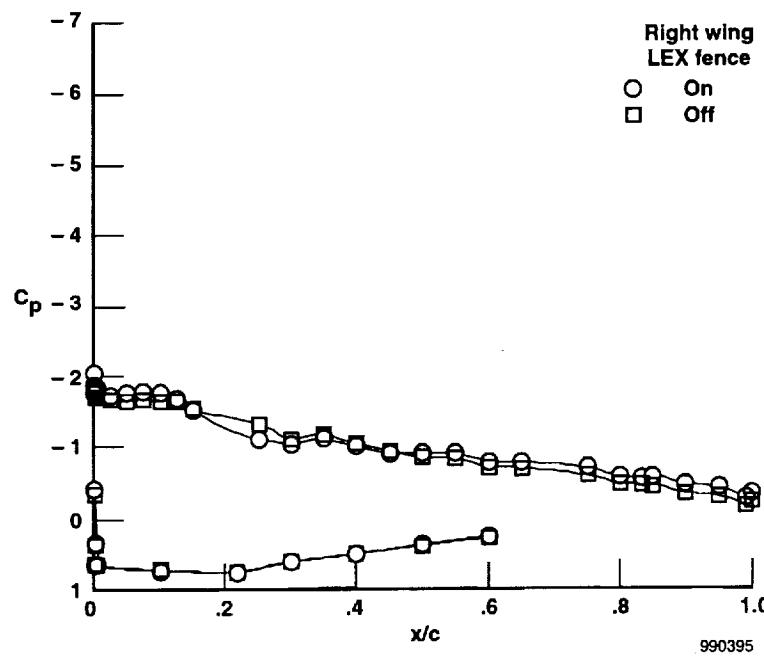
(b) WS 129.

Figure 16. LEX fence effects with $\alpha = 25°$, $\beta = 0°$, $M_\infty = 0.29$, $\delta_{LEF} = 33°$, $\delta_{TEF} = 1°$.
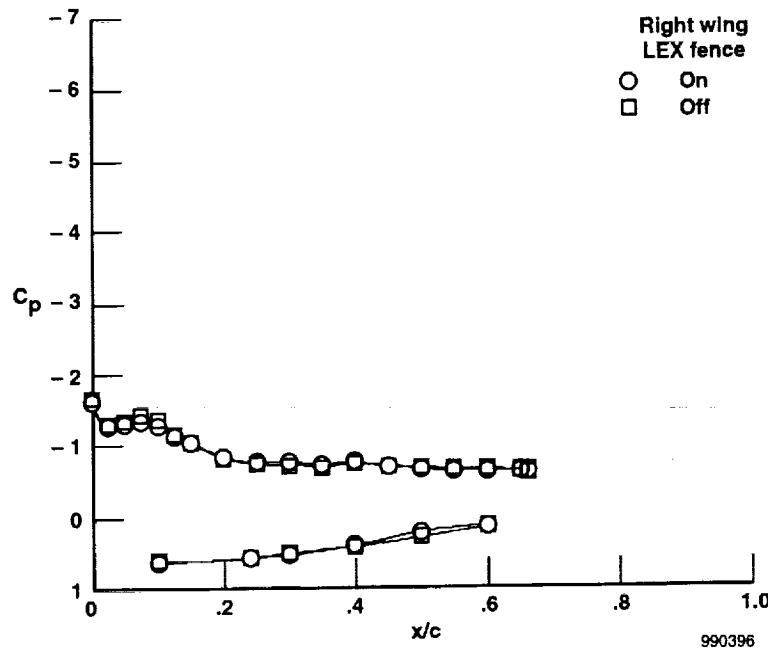
(c) WS 191.

Figure 16. Concluded.
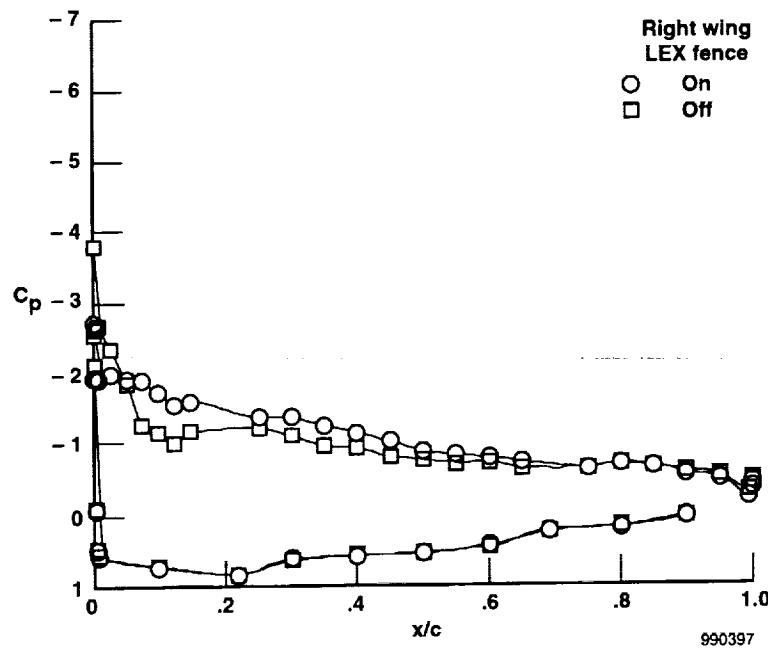
(a) WS 086.

Figure 17. LEX fence effects with $\alpha = 30°$, $\beta = 0°$, $M_\infty = 0.26$, $\delta_{LEF} = 33°$, $\delta_{TEF} = 0°$.
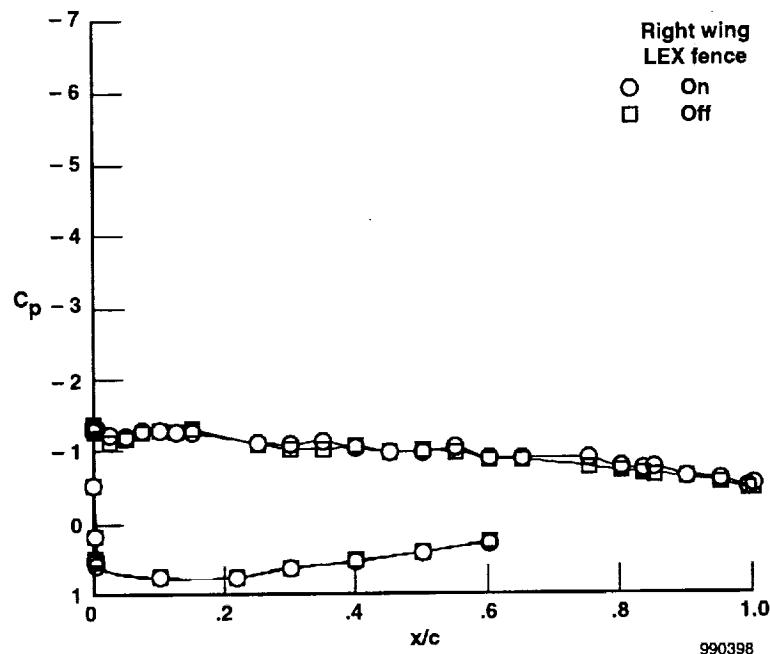
(b) WS 129.
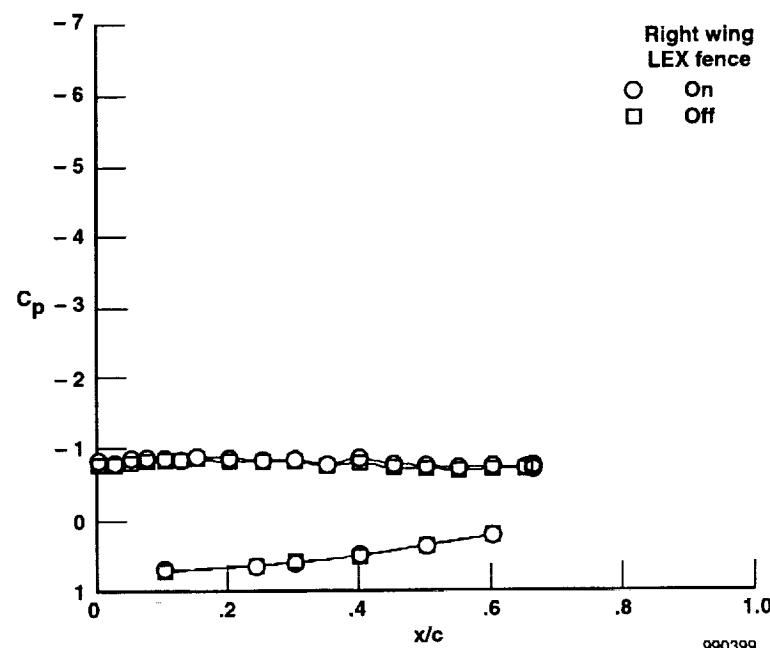
(c) WS 191.

Figure 17. Concluded.
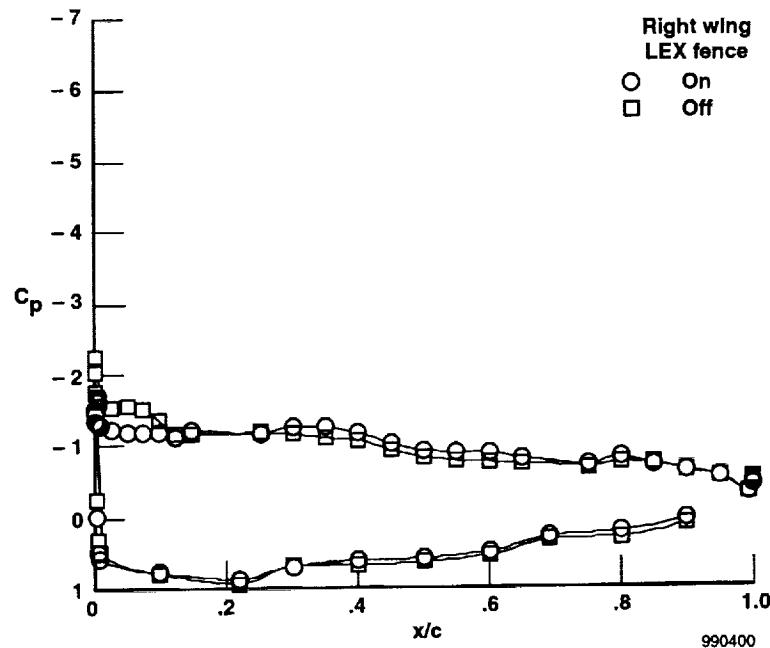
(a) WS 086.
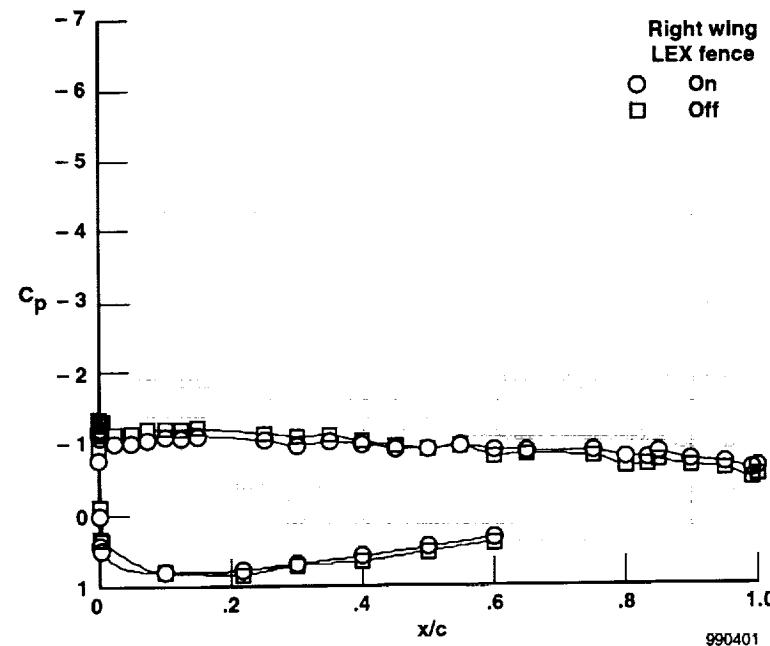
(b) WS 129.

Figure 18. LEX fence effects with $\alpha = 35°$, $\beta = 0°$, $M_\infty = 0.26$, $\delta_{LEF} = 33°$, $\delta_{TEF} = 0°$.
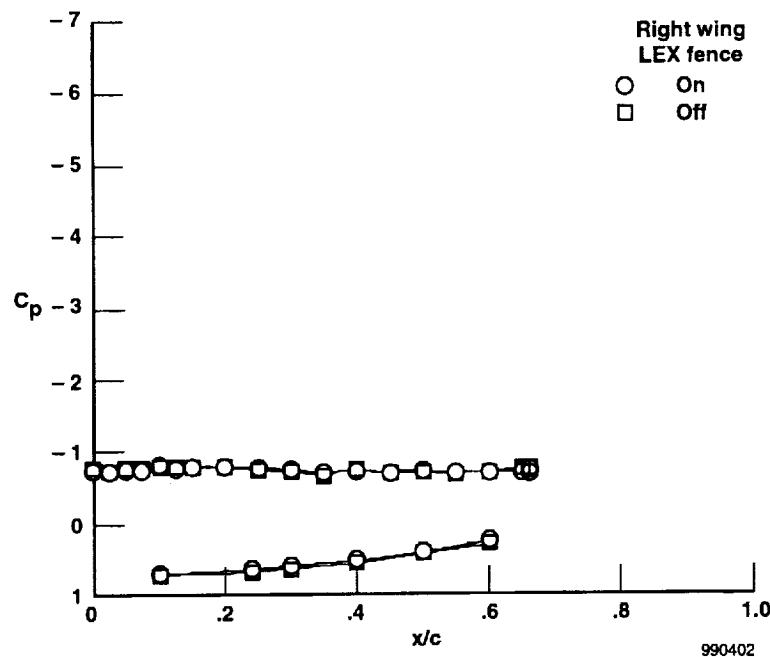
(c) WS 191.

Figure 18. Concluded.
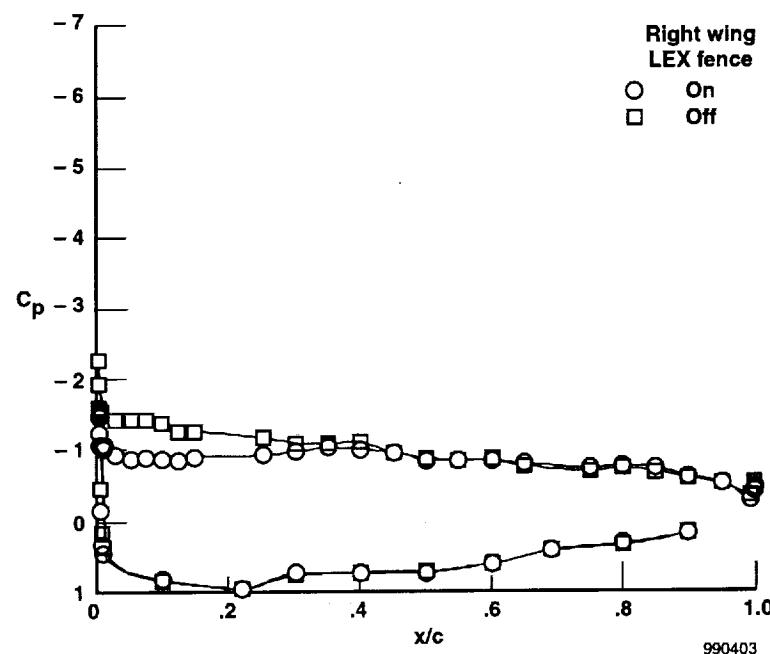
(a) WS 086.

Figure 19. LEX fence effects with $\alpha = 40°$, $\beta = 0°$, $M_\infty = 0.25$, $\delta_{LEF} = 33°$, $\delta_{TEF} = 0°$.
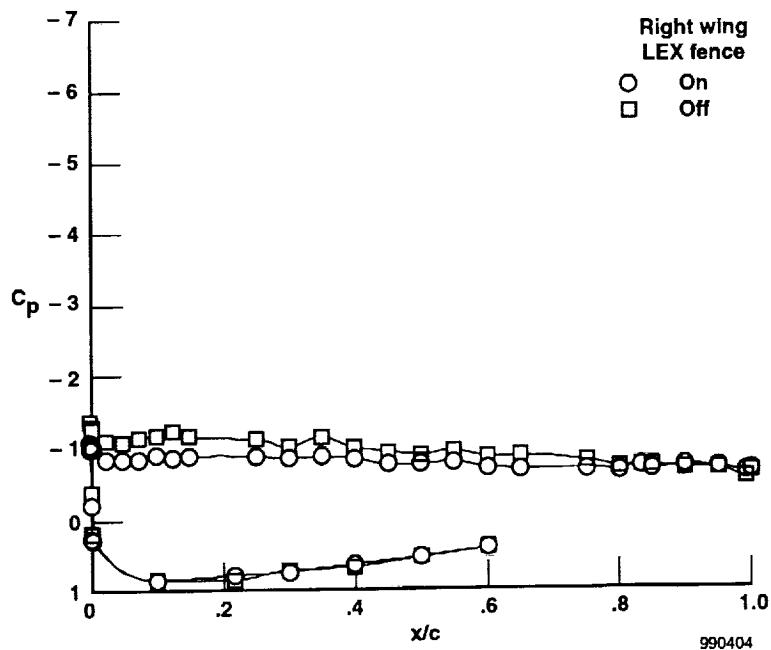
(b) WS 129.
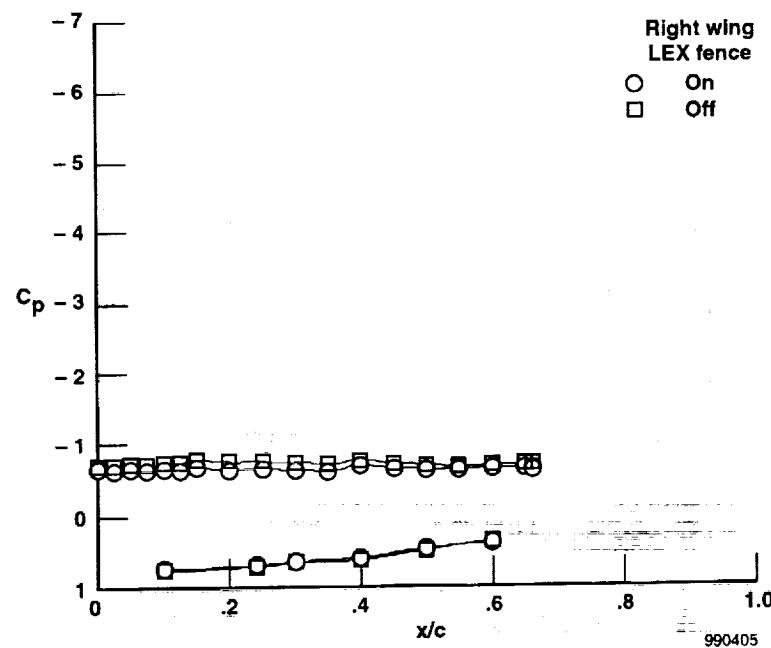
(c) WS 191.

Figure 19. Concluded.

36
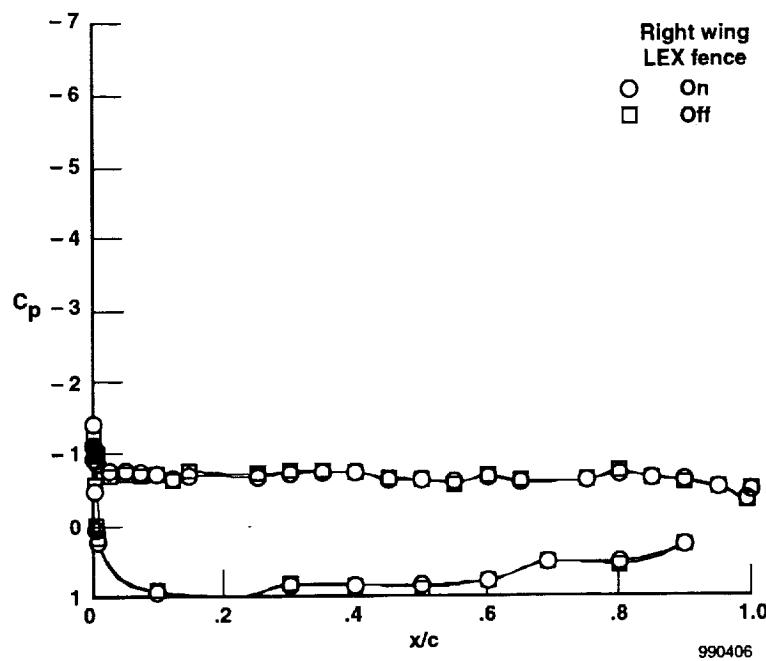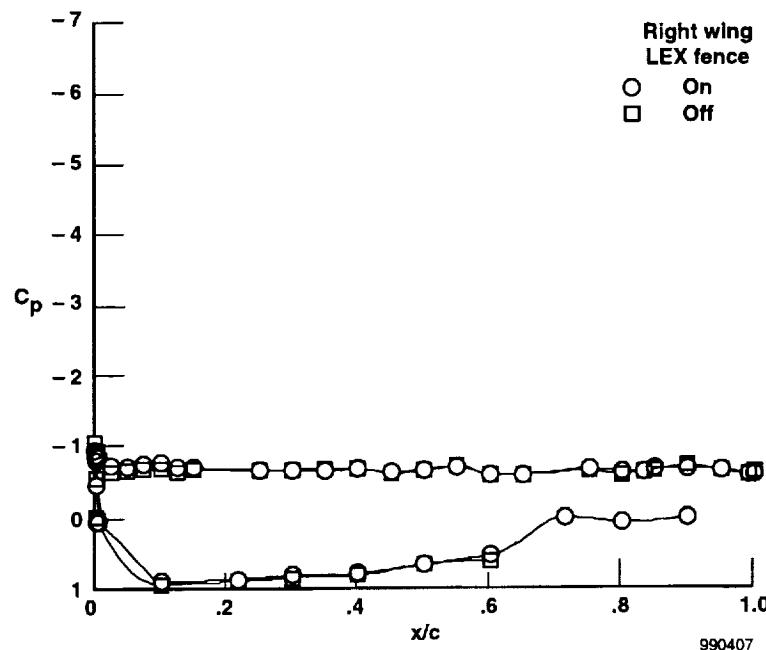
(a) WS 086.

(b) WS 129.

Figure 20. LEX fence effects with $\alpha = 50°$, $\beta = 0°$, $M_\infty = 0.24$, $\delta_{LEF} = 33°$, $\delta_{TEF} = 0°$.
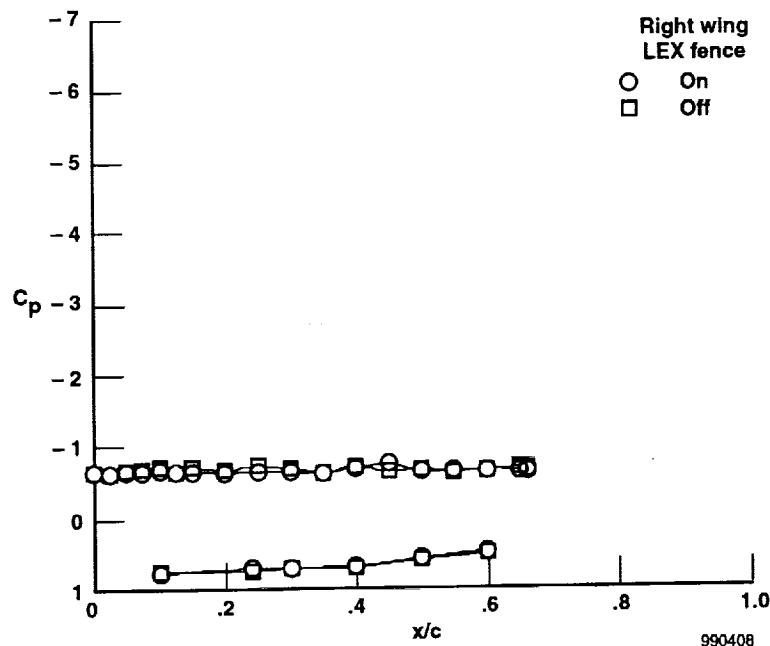
(c) WS 191.

Figure 20. Concluded.
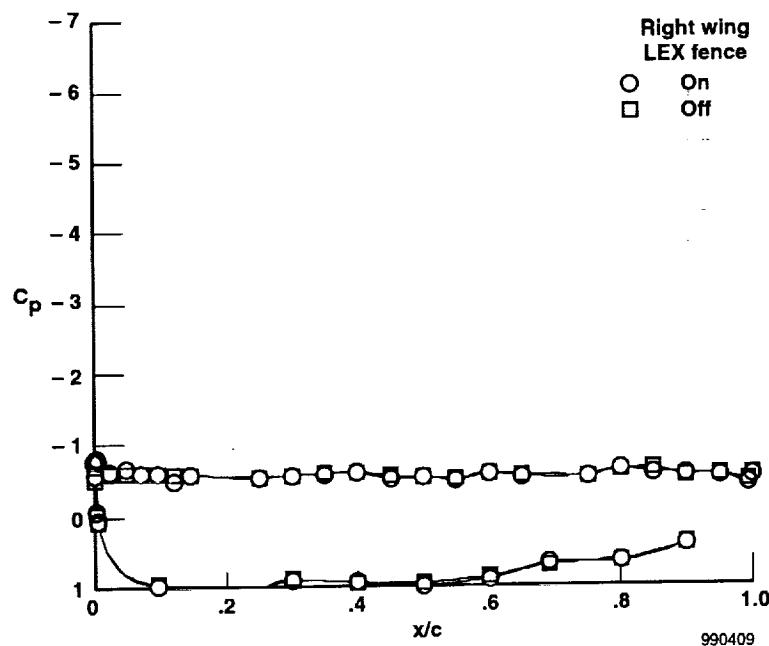
(a) WS 086.

Figure 21. LEX fence effects with $\alpha = 60°$, $\beta = 0°$, $M_\infty = 0.25$, $\delta_{LEF} = 33°$, $\delta_{TEF} = 0°$.

38
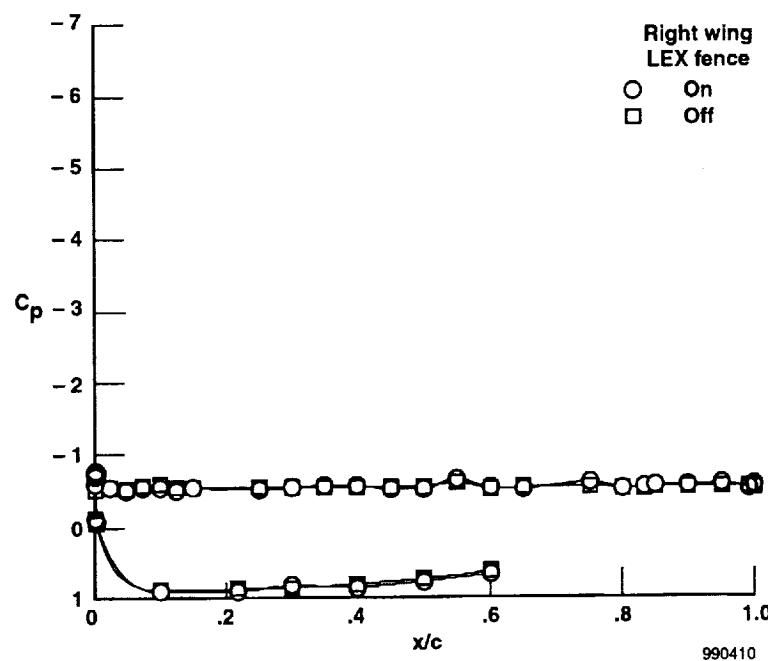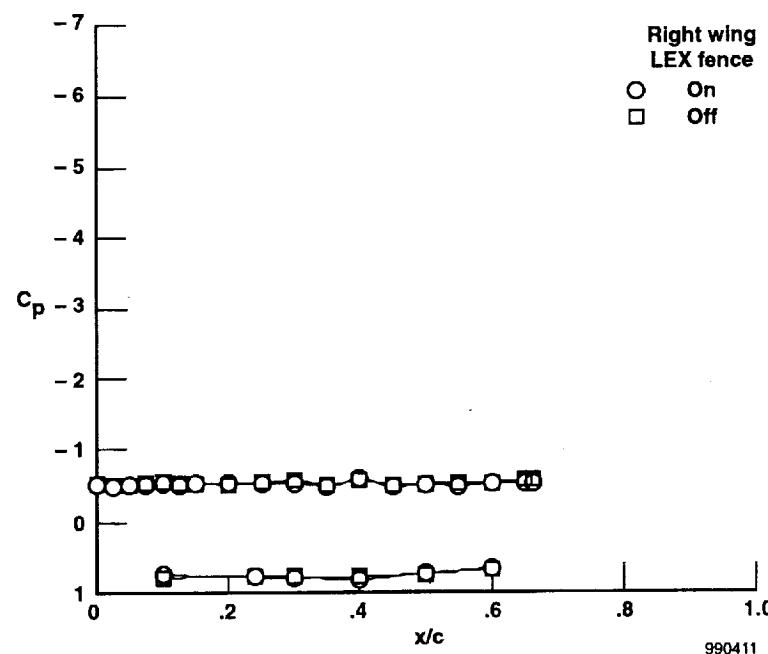
(b) WS 129.

(c) WS 191.

Figure 21. Concluded.
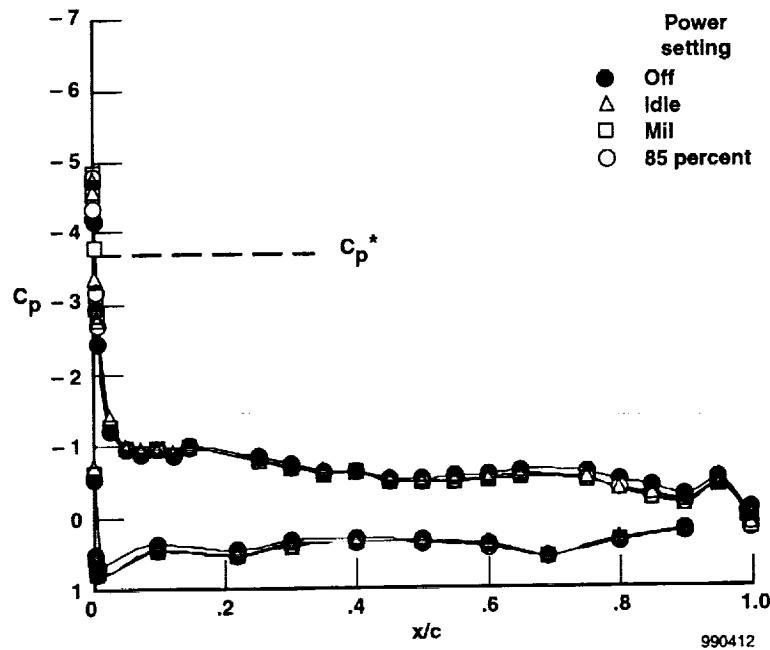
(a) WS 086.
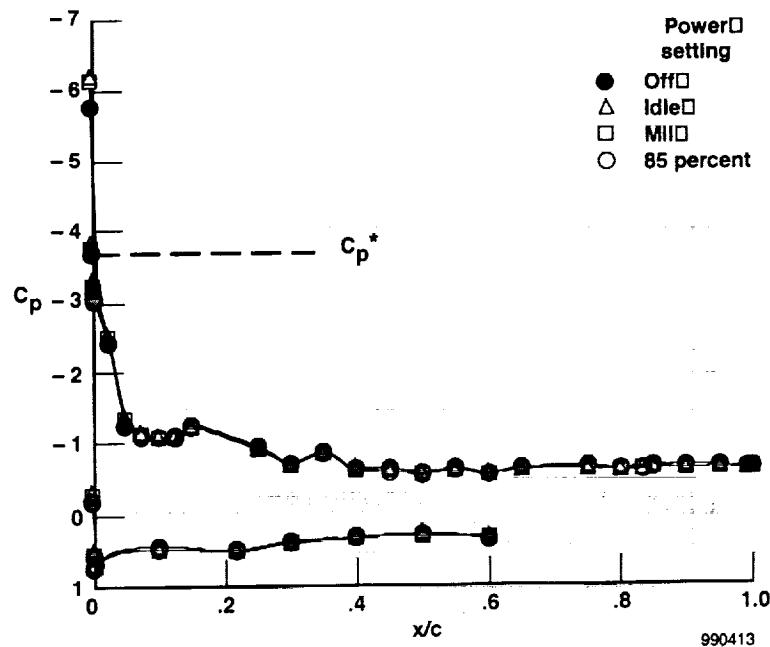
(b) WS 129.

Figure 22. Engine effects on right wing pressure distribution with $\alpha = 11°$, $\beta = 0.7°$, $M_\infty = 0.4$, $\delta_{LEF} = 14°$, $\delta_{TEF} = 16°$.
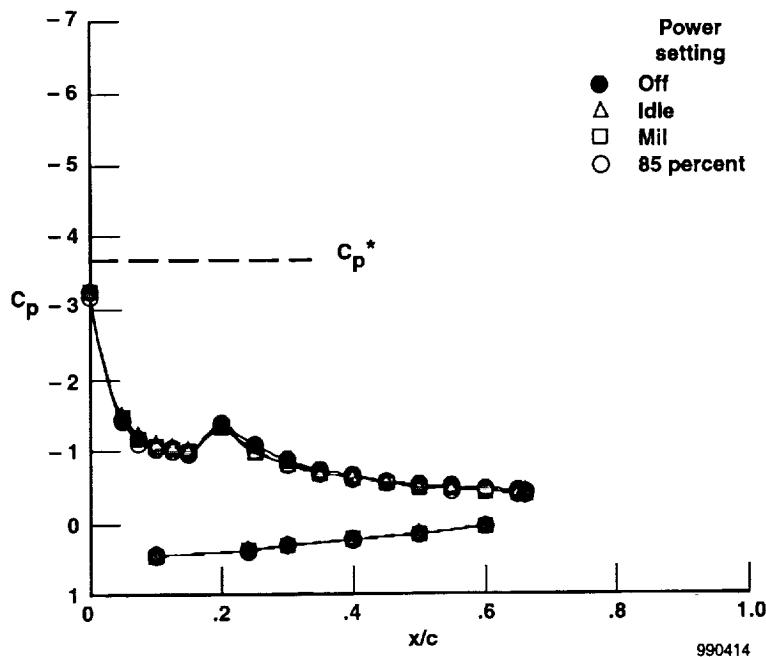
(c) WS 191.

Figure 22. Concluded.
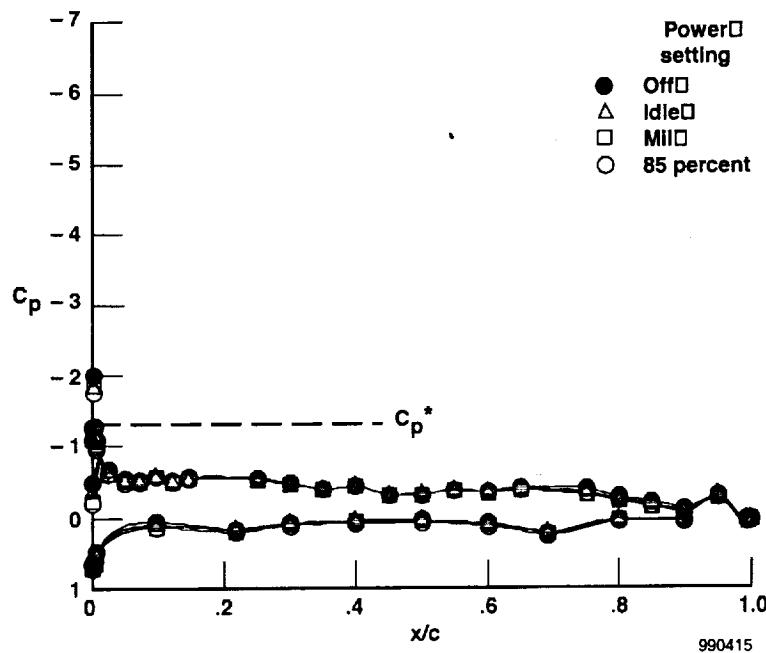
(a) WS 086.

Figure 23. Engine effects on right wing pressure distribution with $\alpha = 5°$, $\beta = 0.2°$, $M_\infty = 0.6$, $\delta_{LEF} = 6°$, $\delta_{TEF} = 7°$.

41
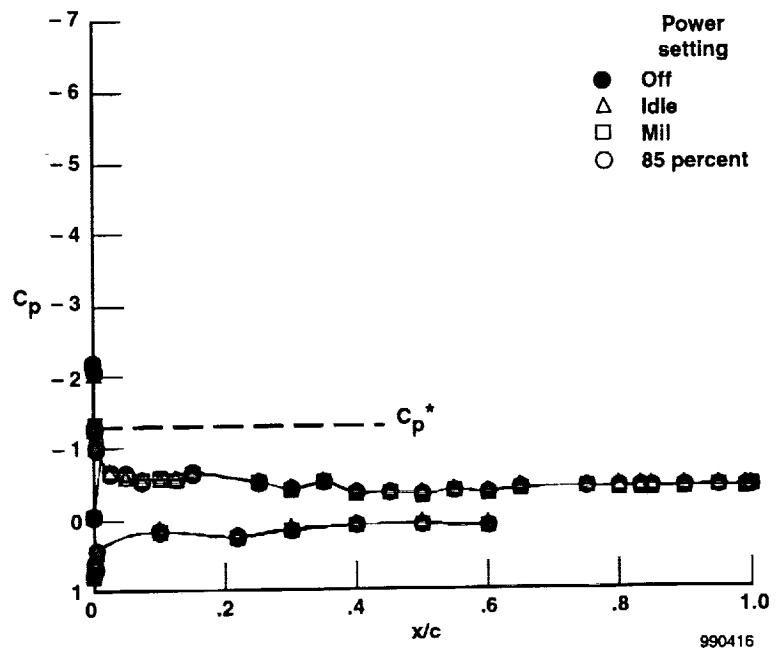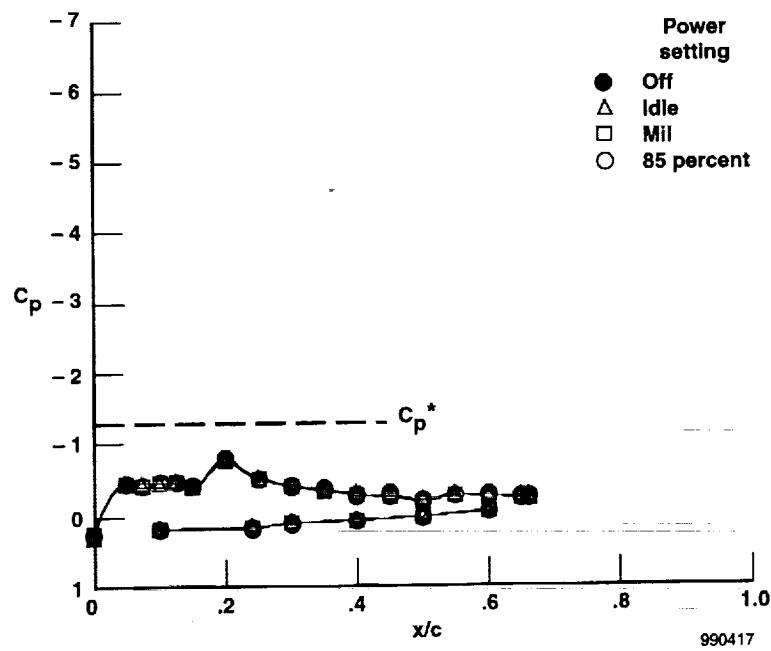
(b) WS 129.

(c) WS 191.

Figure 23. Concluded.

42
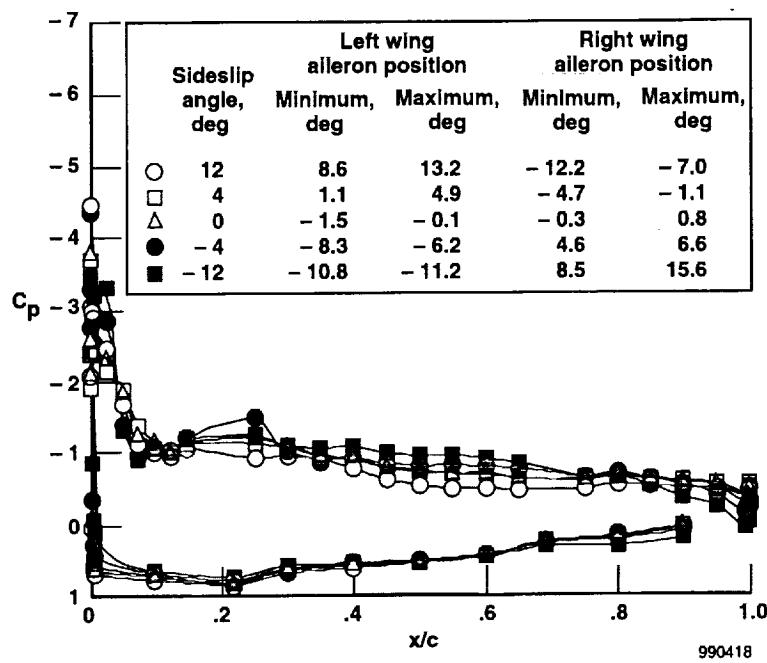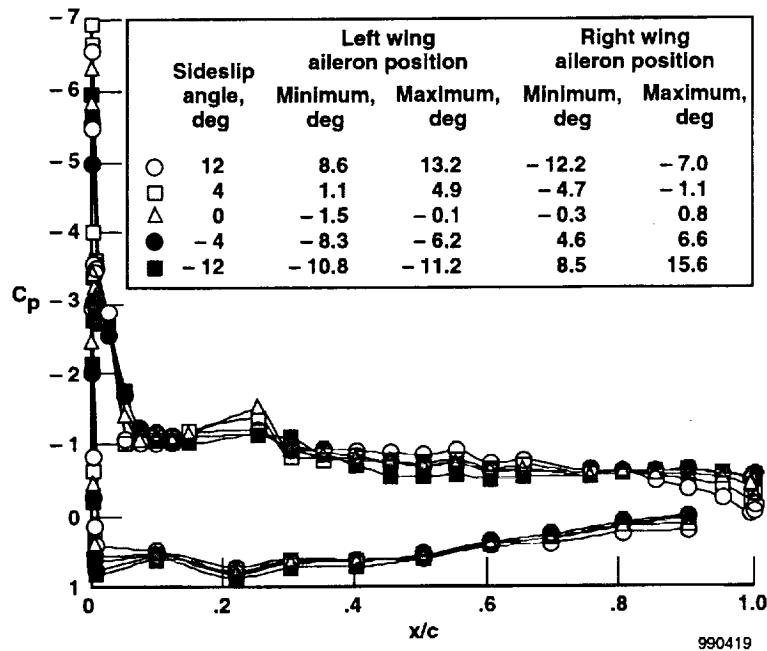
(a) Right wing.

(b) Left wing.

Figure 24. Engine effects of sideslip on pressure distribution at WS 086 with $\alpha = 30°$, $M_\infty = 0.27$, $\delta_{LEF} = 33°$, $\delta_{TEF} = 0°$.

43
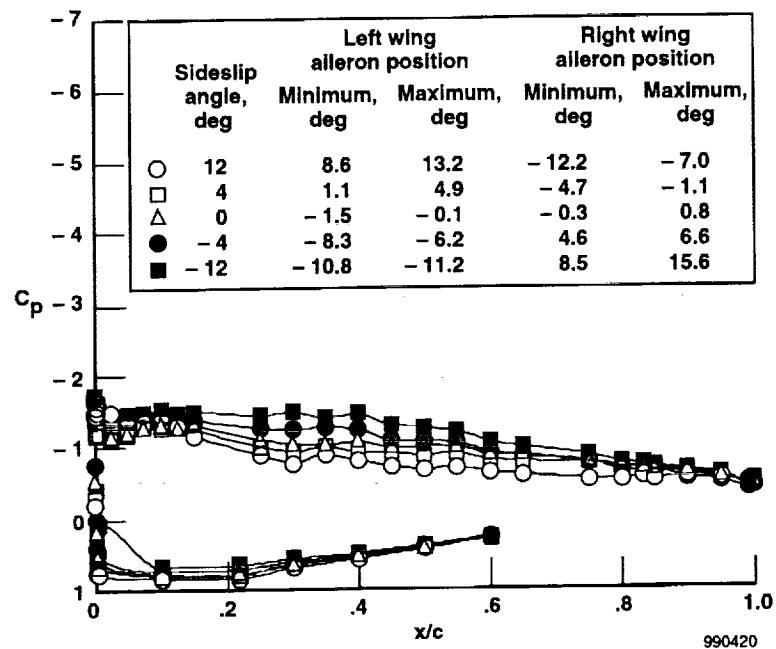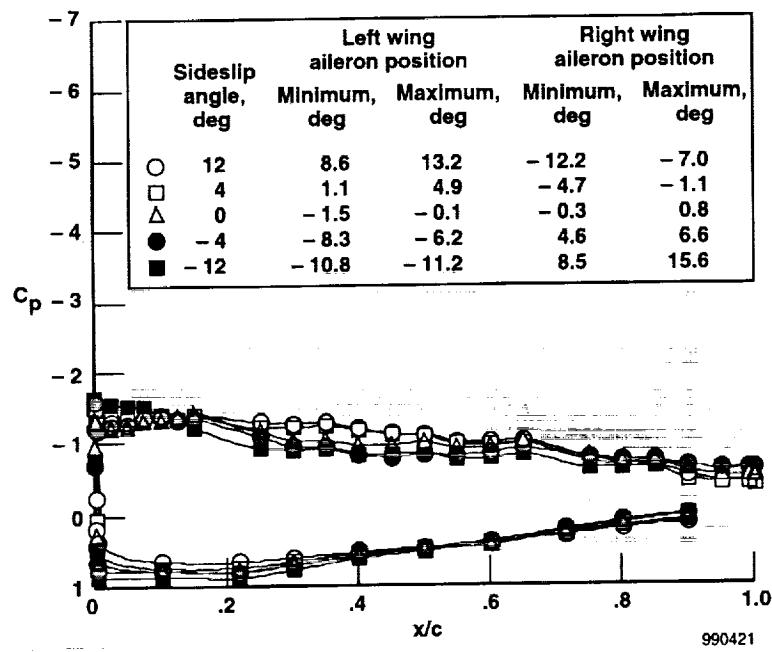
(a) Right wing.

(b) Left wing.

Figure 25. Engine effects of sideslip on pressure distribution at WS 129 with $\alpha = 30°$, $M_\infty = 0.27$, $\delta_{LEF} = 33°$, $\delta_{TEF} = 0°$.
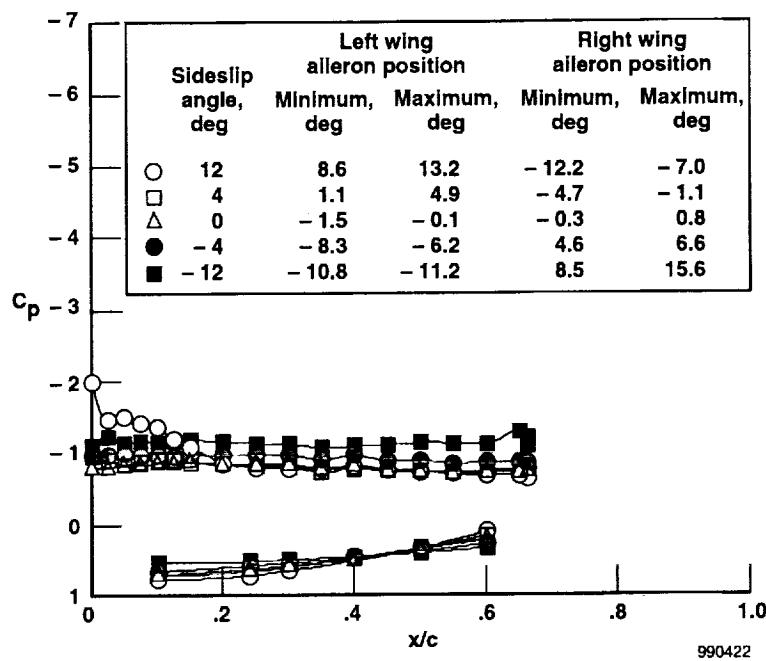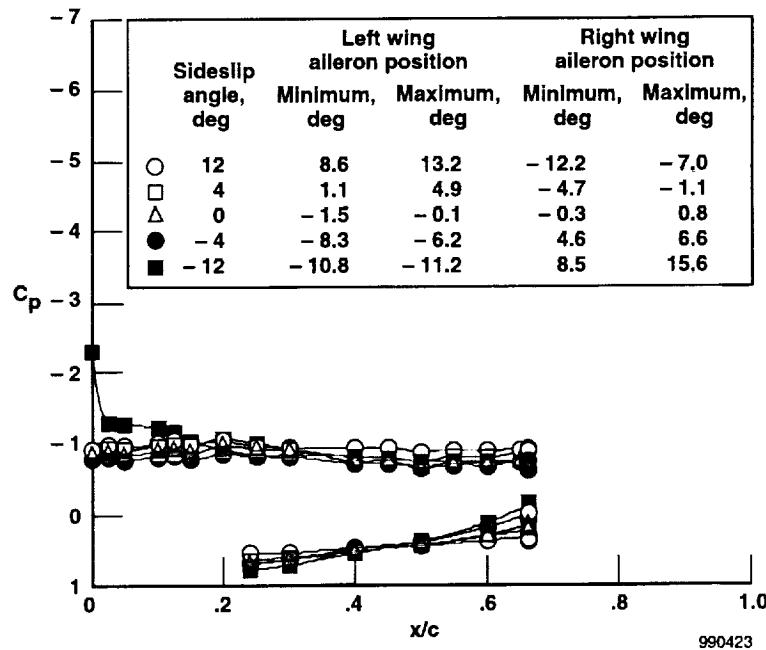
(a) Right wing.

(b) Left wing.

Figure 26. Engine effects of sideslip on pressure distribution at WS 191 with $\alpha = 30°$, $M_\infty = 0.27$, $\delta_{LEF} = 33°$, $\delta_{TEF} = 0°$.
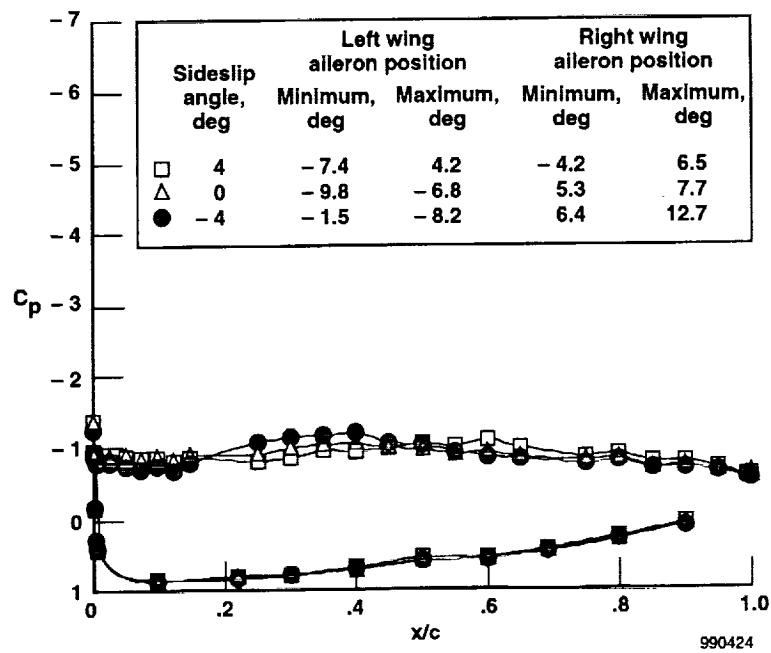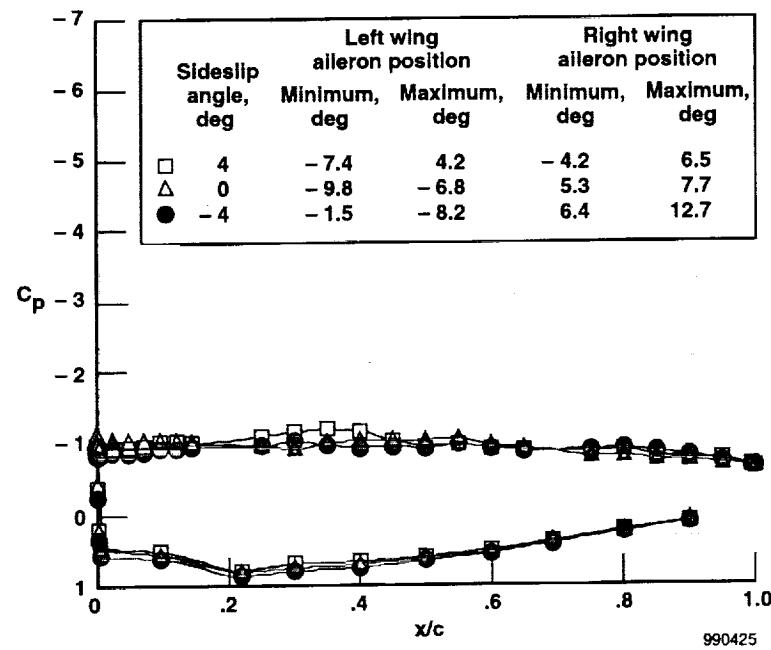
(a) Right wing.

(b) Left wing.

Figure 27. Effects of sideslip on pressure distribution at WS 086 with $\alpha = 45°$, $\beta = 0°$, $M_\infty = 0.23$, $\delta_{LEF} = 33°$, $\delta_{TEF} = 0°$.

(a) Right wing

Sideslip angle, deg	Left wing aileron position		Right wing aileron position	
	Minimum, deg	Maximum, deg	Minimum, deg	Maximum, deg
□ 4	−7.4	4.2	−4.2	6.5
△ 0	−9.8	−6.8	5.3	7.7
● −4	−1.5	−8.2	6.4	12.7

C_p

x/c

990426

(a) Right wing.

(b) Left wing

Sideslip angle, deg	Left wing aileron position		Right wing aileron position	
	Minimum, deg	Maximum, deg	Minimum, deg	Maximum, deg
□ 4	−7.4	4.2	−4.2	6.5
△ 0	−9.8	−6.8	5.3	7.7
● −4	−1.5	−8.2	6.4	12.7

C_p

x/c

990427
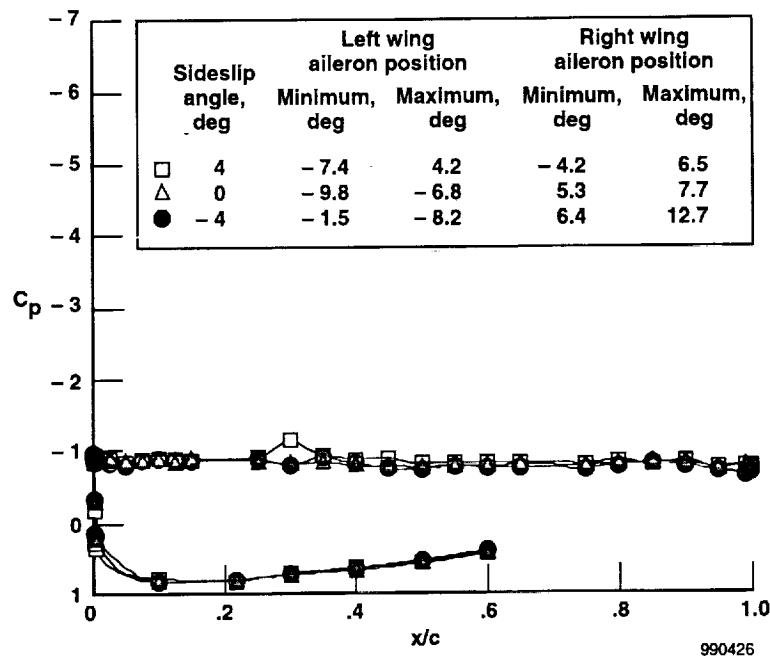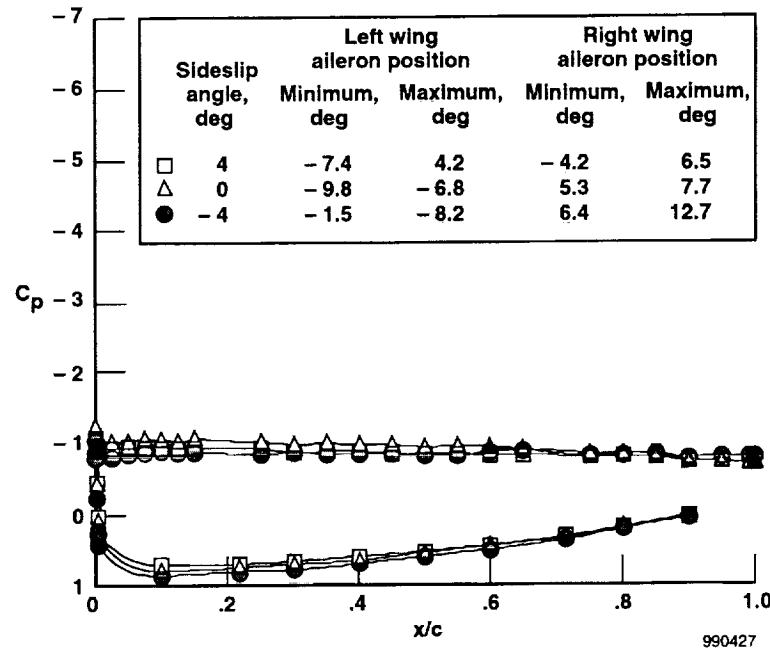
(b) Left wing.

Figure 28. Effects of sideslip on pressure distribution at WS 129 with $\alpha = 45°$, $\beta = 0°$, $M_\infty = 0.23$, $\delta_{LEF} = 33°$, $\delta_{TEF} = 0°$.

47
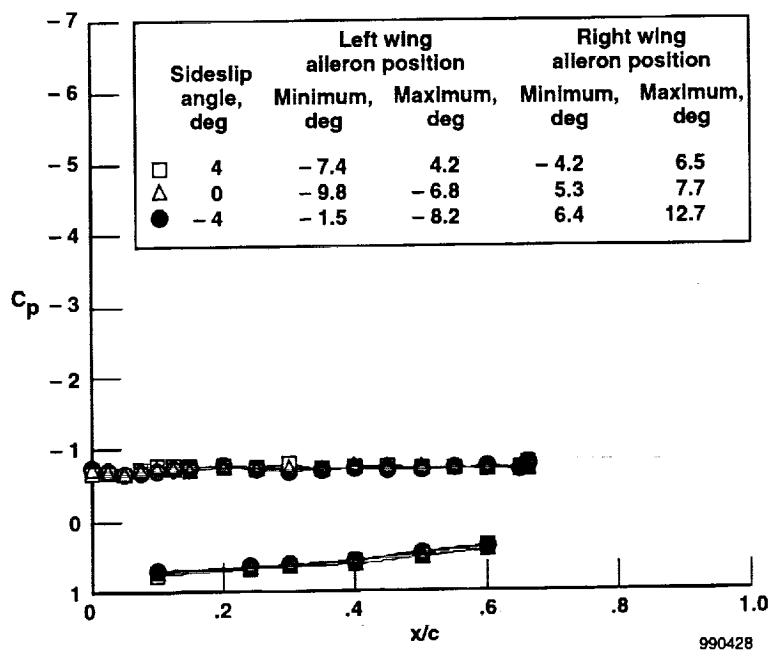
(a) Right wing.

(b) Left wing.

Figure 29. Effects of sideslip on pressure distribution at WS 191 with $\alpha = 45°$, $\beta = 0°$, $M_\infty = 0.23$, $\delta_{LEF} = 33°$, $\delta_{TEF} = 0°$.

48
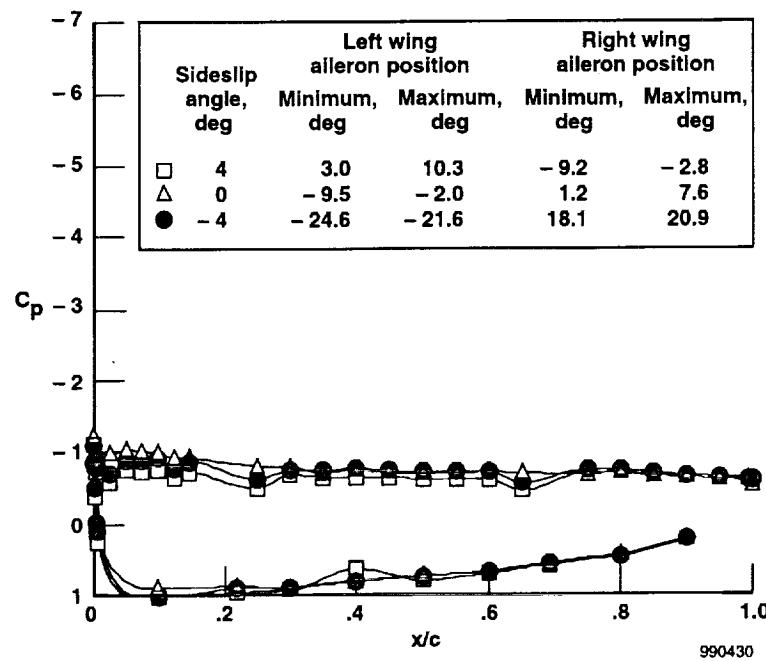
(a) Right wing.

(b) Left wing.

Figure 30. Effects of sideslip on pressure distribution at WS 086 with $\alpha = 55°$, $\beta = 0°$, $M_\infty = 0.25$, $\delta_{LEF} = 33°$, $\delta_{TEF} = 0°$.
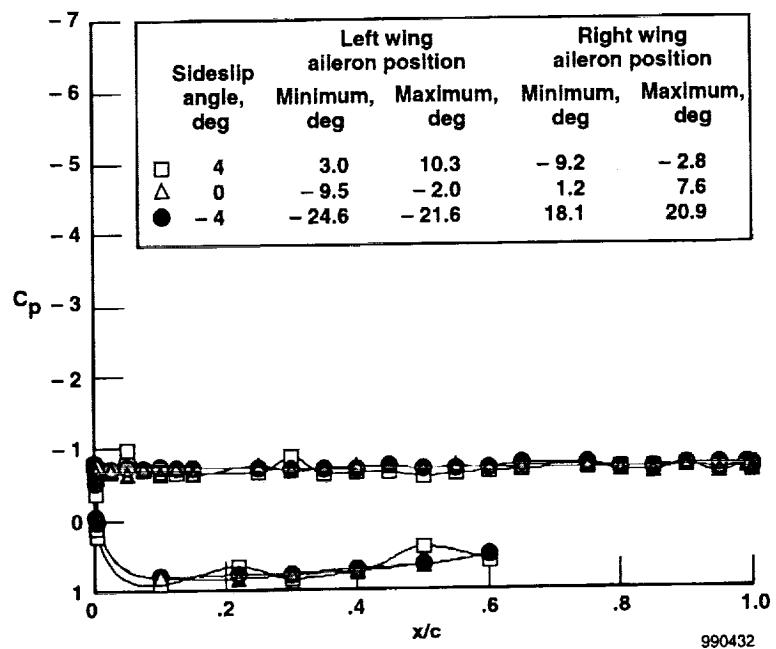
(a) Right wing.
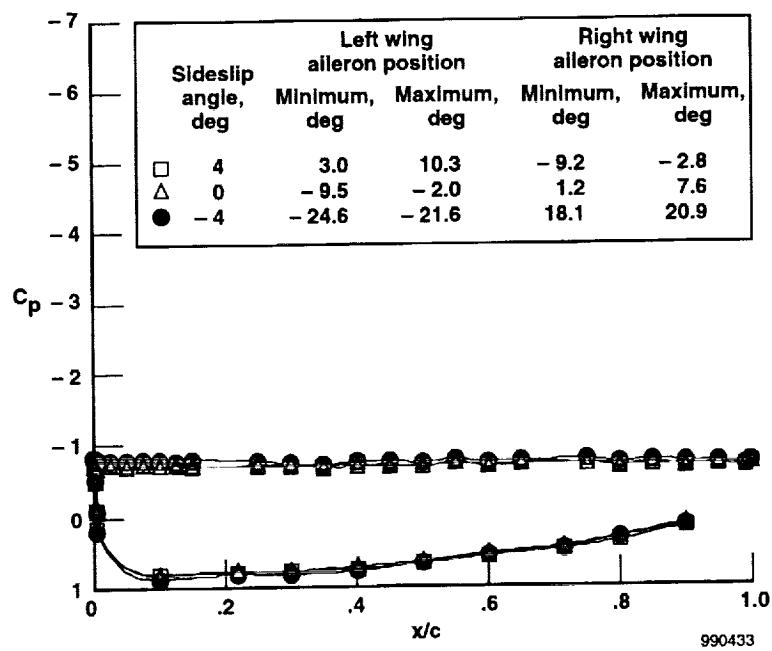
(b) Left wing.

Figure 31. Effects of sideslip on pressure distribution at WS 129 with $\alpha = 55°$, $\beta = 0°$, $M_\infty = 0.25$, $\delta_{LEF} = 33°$, $\delta_{TEF} = 0°$.

50
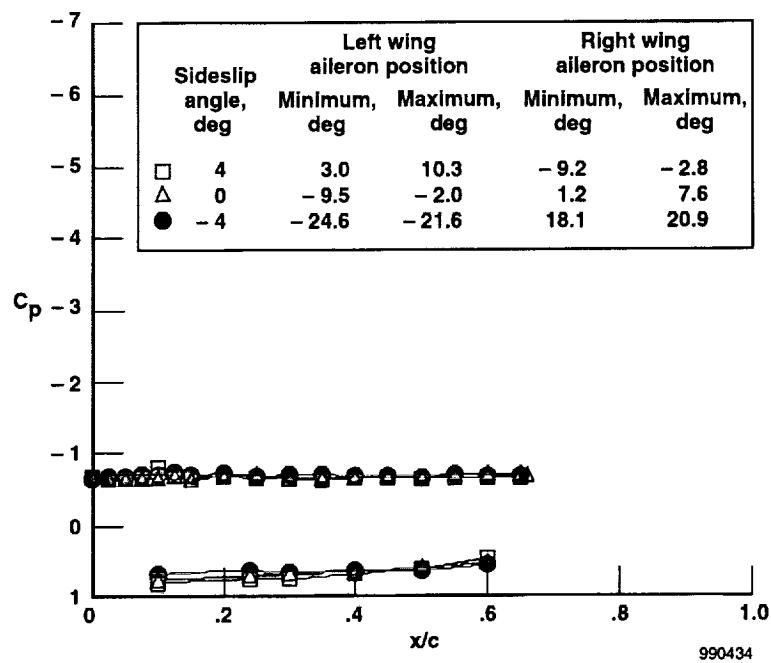
(a) Right wing.
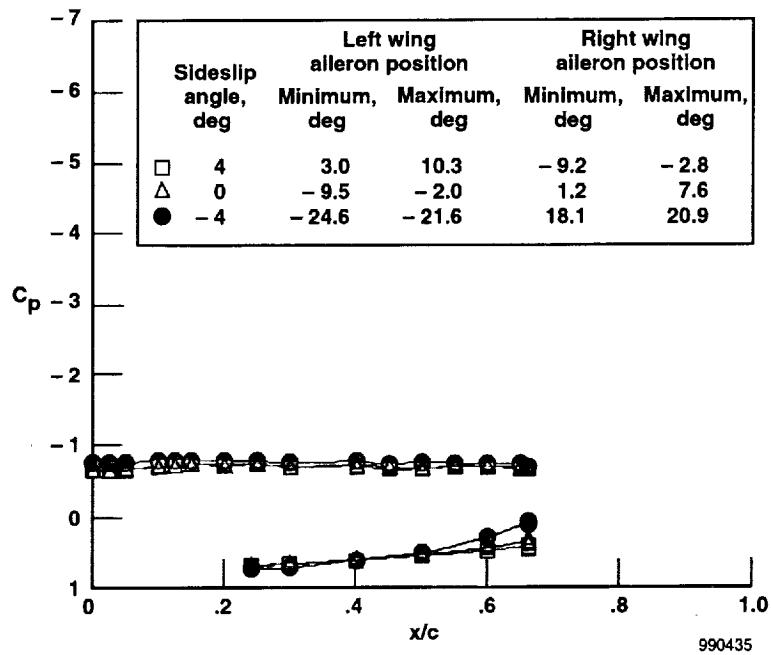
(b) Left wing.

Figure 32. Effects of sideslip on pressure distribution at WS 191 with $\alpha = 55°$, $\beta = 0°$, $M_\infty = 0.25$, $\delta_{LEF} = 33°$, $\delta_{TEF} = 0°$.

51
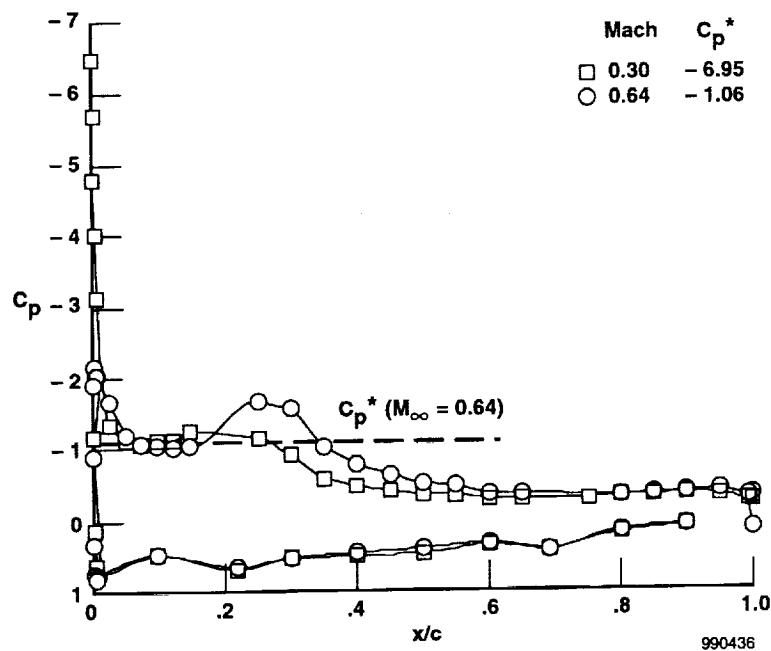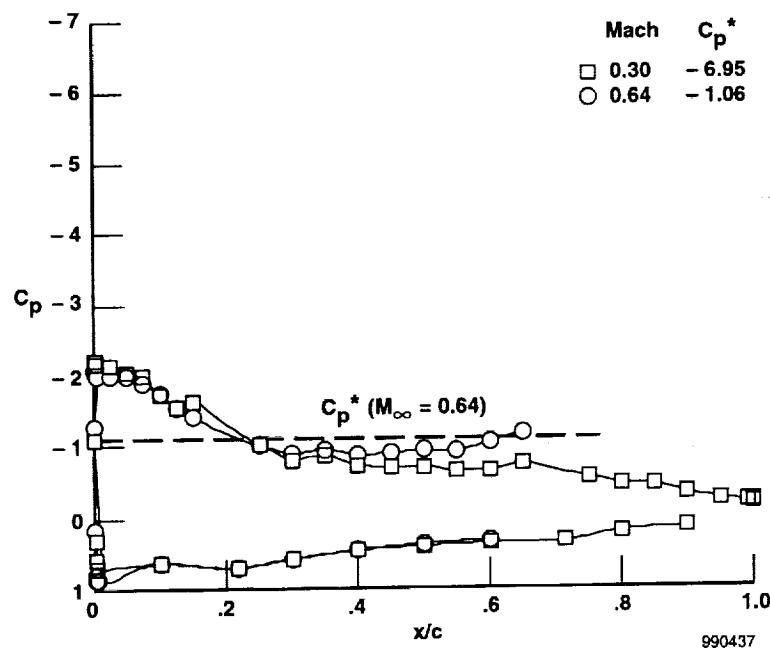
(a) WS 086.

(b) WS 129.

Figure 33. Effects of Mach number on pressure distribution with $\alpha = 20°$, $\beta = 0°$, $\delta_{LEF} = 27°$, $\delta_{TEF} = 8°$.
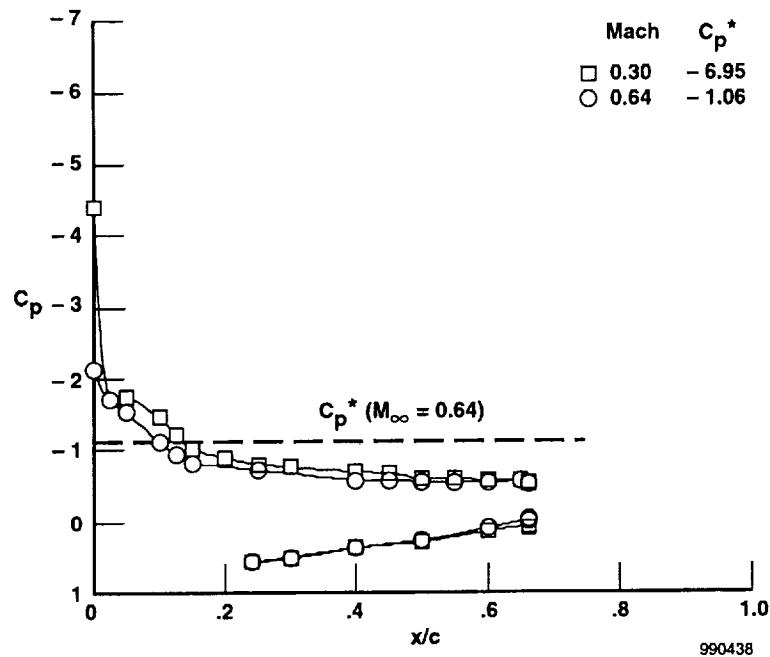
(c) WS 191.

Figure 33. Concluded.
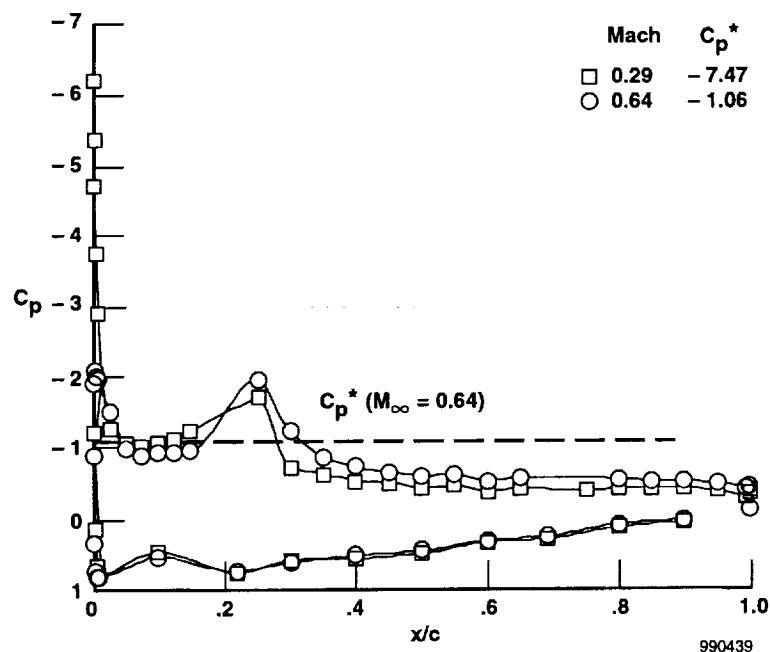
(a) WS 086.

Figure 34. Effects of Mach number on pressure distribution with $\alpha = 25°$, $\beta = 0°$, $\delta_{LEF} = 33°$, $\delta_{TEF} = 0°$.
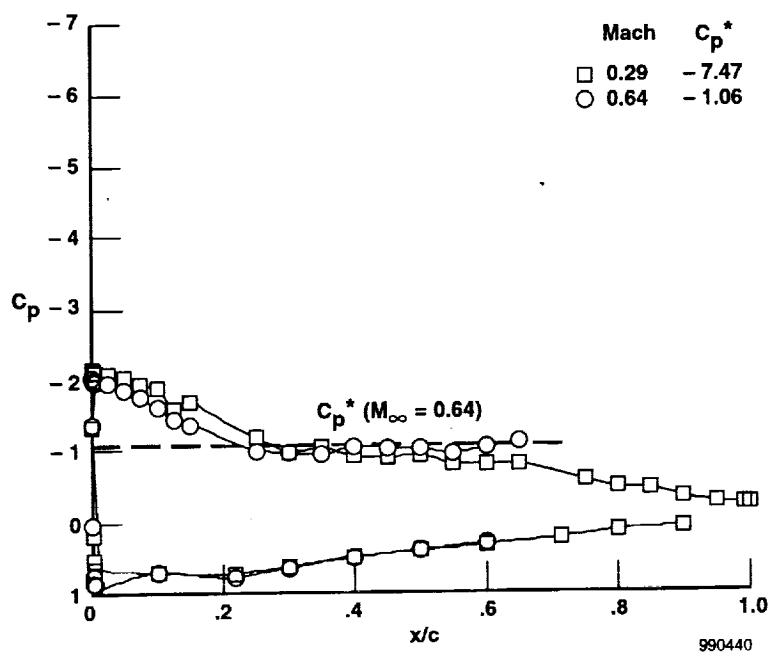
(b) WS 129.
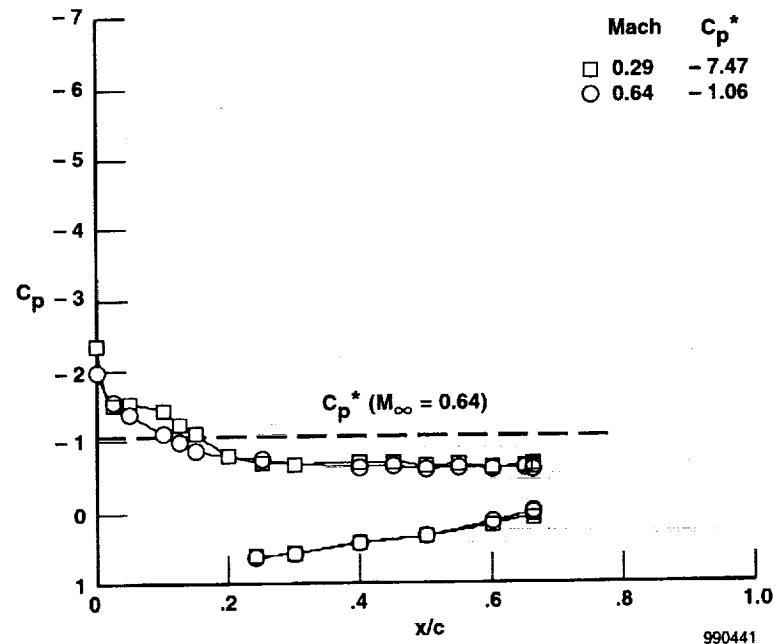
(c) WS 191.

Figure 34. Concluded.
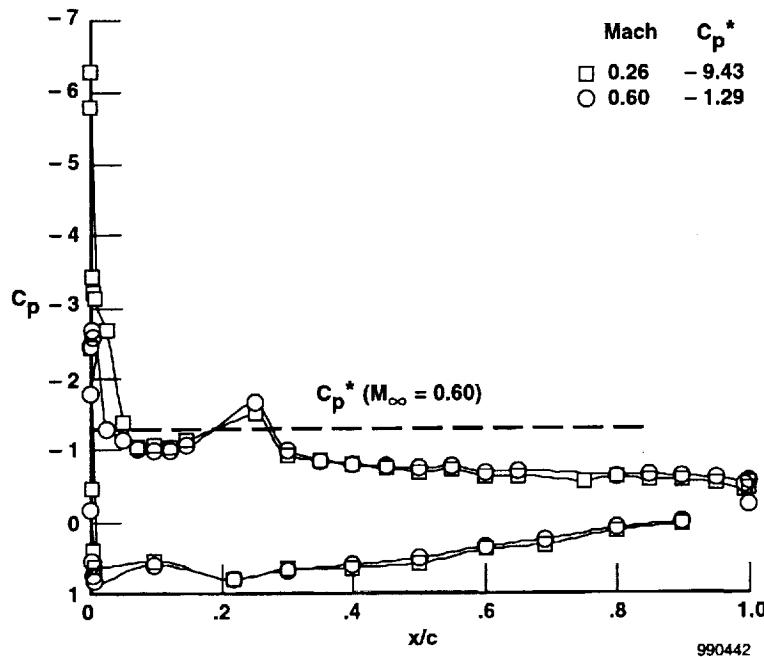
(a) WS 086.
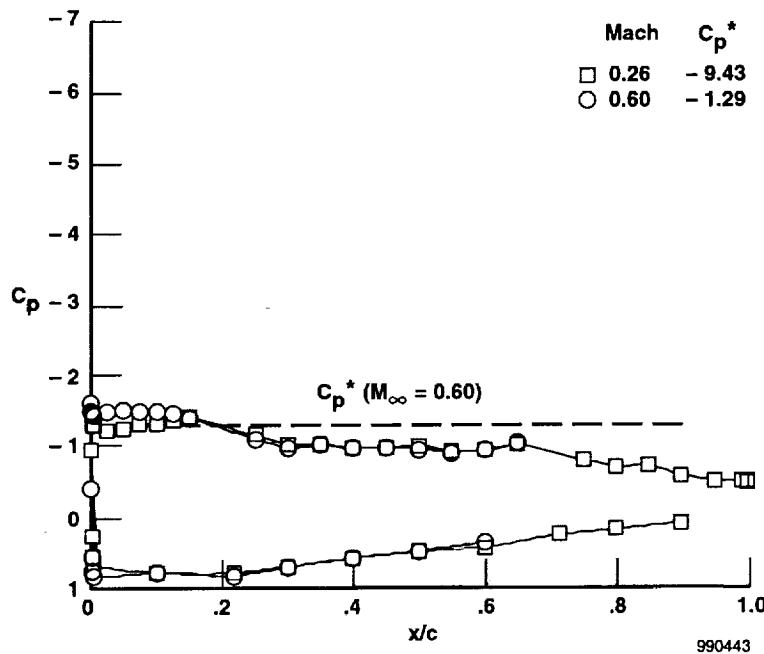
(b) WS 129.

Figure 35. Effects of Mach number on pressure distribution with $\alpha = 30°$, $\beta = 0°$, $\delta_{LEF} = 33°$, $\delta_{TEF} = 0°$.

55
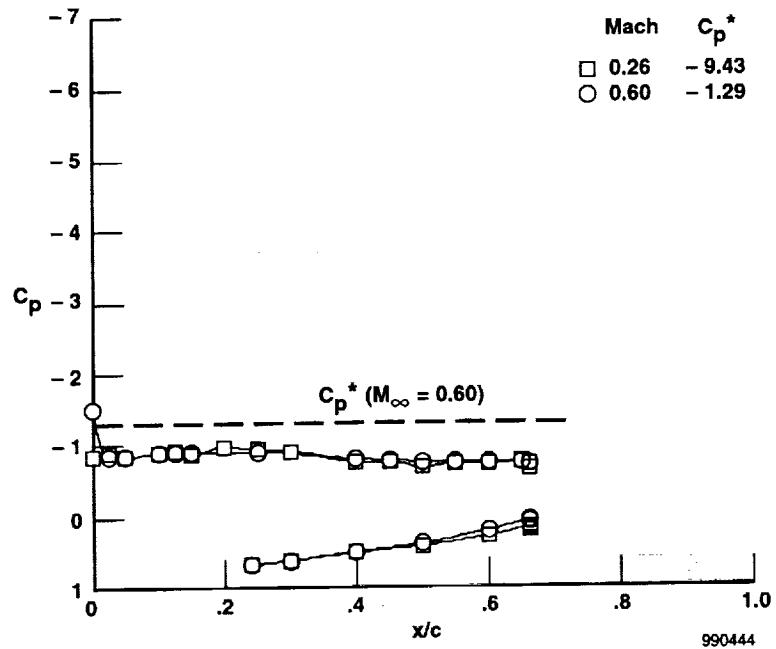
(c) WS 191.

Figure 35. Concluded.
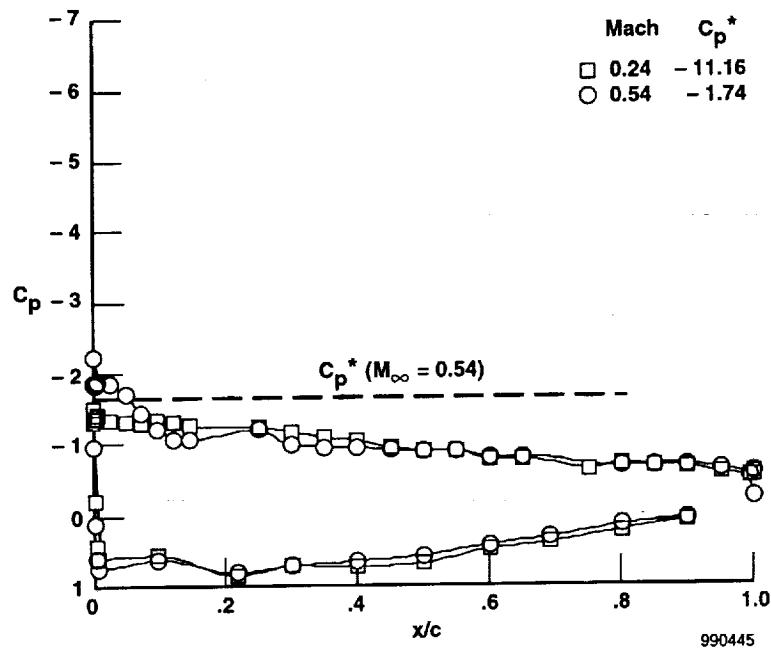
(a) WS 086.

Figure 36. Effects of Mach number on pressure distribution with $\alpha = 35°$, $\beta = 0.4°$, $\delta_{LEF} = 33°$, $\delta_{TEF} = 0°$.
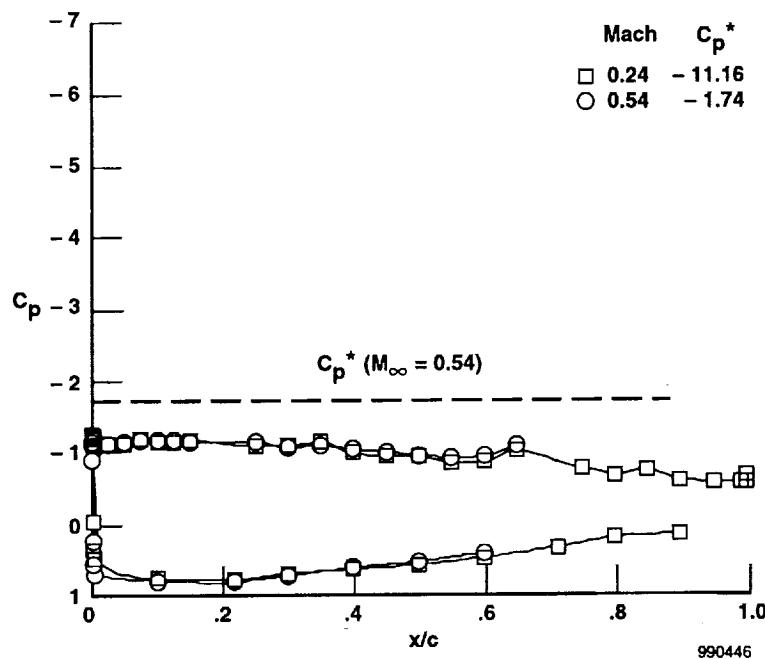
(b) WS 129.
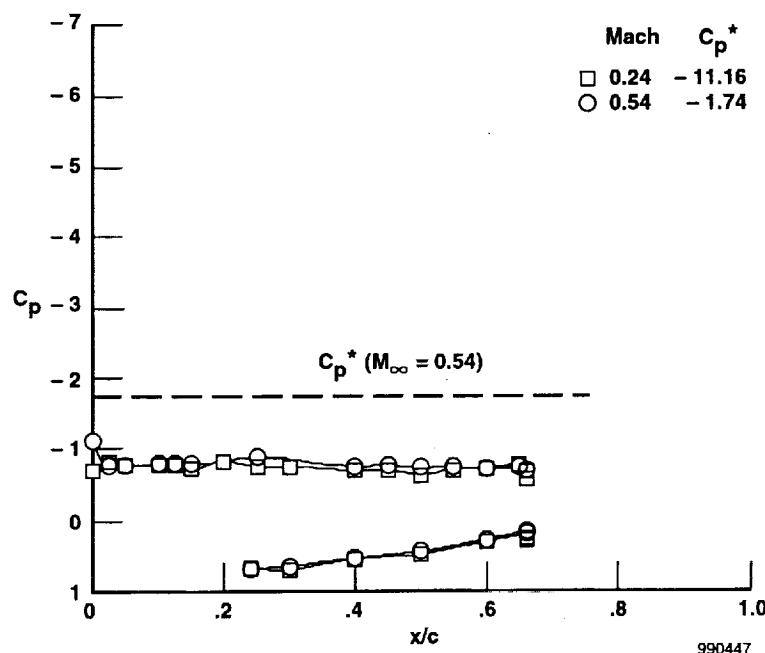
(c) WS 191.

Figure 36. Concluded.

REPORT DOCUMENTATION PAGE

1. AGENCY USE ONLY (Leave blank)	2. REPORT DATE	3. REPORT TYPE AND DATES COVERED
	March 2000	Technical Paper

4. TITLE AND SUBTITLE

In-Flight Wing Pressure Distributions for the NASA F/A-18A High Alpha Research Vehicle

5. FUNDING NUMBERS

WU 529-55-24-E8-RR-00-000

6. AUTHOR(S)

Mark C. Davis and John A. Saltzman

7. PERFORMING ORGANIZATION NAME(S) AND ADDRESS(ES)

NASA Dryden Flight Research Center
P.O. Box 273
Edwards, California 93523-0273

8. PERFORMING ORGANIZATION REPORT NUMBER

H-2389

9. SPONSORING/MONITORING AGENCY NAME(S) AND ADDRESS(ES)

National Aeronautics and Space Administration
Washington, DC 20546-0001

10. SPONSORING/MONITORING AGENCY REPORT NUMBER

NASA/TP-2000-209018

11. SUPPLEMENTARY NOTES

12a. DISTRIBUTION/AVAILABILITY STATEMENT

Unclassified—Unlimited
Subject Category 02, 05

This report is available at http://www.dfrc.nasa.gov/DTRS/

12b. DISTRIBUTION CODE

13. ABSTRACT (Maximum 200 words)

Pressure distributions on the wings of the F/A-18A High Alpha Research Vehicle (HARV) were obtained using both flush-mounted pressure orifices and surface-mounted pressure tubing. During quasi-stabilized 1-g flight, data were gathered at ranges for angle of attack from 5° to 70°, for angle of sideslip from –12° to +12°, and for Mach from 0.23 to 0.64, at various engine settings, and with and without the leading edge extension fence installed. Angle of attack strongly influenced the wing pressure distribution, as demonstrated by a distinct flow separation pattern that occurred between the range from 15° to 30°. Influence by the leading edge extension fence was evident on the inboard wing pressure distribution, but little influence was seen on the outboard portion of the wing. Angle-of-sideslip influence on wing pressure distribution was strongest at low angle of attack. Influence of Mach number was observed in the regions of local supersonic flow, diminishing as angle of attack was increased. Engine throttle setting had little influence on the wing pressure distribution.

14. SUBJECT TERMS

F-18, Flight test, Flow visualization, Lift, Pressure distribution, Separation, Wing pressures

15. NUMBER OF PAGES

63

16. PRICE CODE

A04

17. SECURITY CLASSIFICATION OF REPORT	18. SECURITY CLASSIFICATION OF THIS PAGE	19. SECURITY CLASSIFICATION OF ABSTRACT	20. LIMITATION OF ABSTRACT
Unclassified	Unclassified	Unclassified	Unlimited